MNRAS **452,** 2149–2167 (2015) doi:10.1093/mnras/stv1288

Combining spectroscopic and photometric surveys using angular cross-correlations – I. Algorithm and modelling

Martin Eriksen[1,2]★ and Enrique Gaztañaga[1]★

[1]*Institut de Ciències de l'Espai (IEEC-CSIC), E-08193 Bellaterra (Barcelona), Spain*
[2]*Leiden Observatory, Leiden University, PO Box 9513, NL-2300 RA Leiden, the Netherlands*

Accepted 2015 June 8. Received 2015 May 10; in original form 2014 December 25

ABSTRACT

Weak lensing (WL) clustering is studied using 2D (angular) coordinates, while redshift space distortions (RSD) and baryon acoustic oscillations (BAO) use 3D coordinates, which requires a model-dependent conversion of angles and redshifts into comoving distances. This is the first paper of a series, which explore modelling multi-tracer galaxy clustering (of WL, BAO and RSD), using only angular (2D) cross-correlations in thin redshift bins. This involves evaluating many thousands cross-correlations, each a multidimensional integral, which is computationally demanding. We present a new algorithm that performs these calculations as matrix operations. Nearby narrow redshift bins are intrinsically correlated, which can be used to recover the full (radial) 3D information. We show that the Limber approximation does not work well for this task. In the exact calculation, both the clustering amplitude and the RSD effect increase when decreasing the redshift bin width. For narrow bins, the cross-correlation has a larger BAO peak than the auto-correlation because smaller scales are filtered out by the radial redshift separation. Moreover, the BAO peak shows a second (ghost) peak, shifted to smaller angles. We explore how WL, RSD and BAO contribute to the cross-correlations as a function of the redshift bin width and present a first exploration of non-linear effects and signal-to-noise ratio on these quantities. This illustrates that the new approach to clustering analysis provides new insights and is potentially viable in practice.

Key words: cosmological parameters – dark energy – dark matter – large-scale structure of Universe.

1 INTRODUCTION

Galaxy surveys provide data for constraining cosmological models. In the next few years and decades, the constraints will improve from current and upcoming surveys. The completed Canada-France-Hawaii Telescope Legacy Survey (stage II) measured shear in the 155 sq. deg. wide fields to $i < 24.5$ (Fu et al. 2008; Heymans et al. 2013; Kilbinger et al. 2013). The dark energy survey has completed the first year of data and plan to observe 5000 sq. deg. to $i < 24.1$ over the next four years. Another examples of ongoing weak lensing (WL) survey are Kilo Degree Survey, which aim to map about 1500 sq. deg. each to different depths. In the next decade, *Euclid* (Laureijs et al. 2011; Amiaux et al. 2012; Amendola et al. 2013) and LSST (Ivezic et al. 2008; LSST Science Collaboration 2009) will provide the next generation (stage IV) of deep lensing surveys, both covering around 15 000 sq. deg.

For spectroscopic surveys, the VIMOS VLT Deep Survey measured 34 594 galaxies (Le Fèvre et al. 2013), the Wiggle-Z measured almost 240 000 galaxies over 1000 sq. deg. in the redshift range $0.2 < z < 1.0$ (Parkinson et al. 2012), while the BOSS survey mapped the redshift of 1.5 million galaxy to $z \approx 0.7$ in 10 000 sq. deg. (Anderson et al. 2014). A stage IV spectroscopic survey is DESI (Levi et al. 2013), which is a merger of the previous BigBoss (Schlegel et al. 2009, 2011) and DESpec collaborations (Abdalla et al. 2012). Expected to start in 2018 at the Mayall telescope, DESI aims at measuring redshift space distortions (RSD) and baryon acoustic oscillations (BAO) through targeting 20 million galaxies and covers between 14 000 to 18 000 sq. deg. Also, a new generation of narrow-band cosmological surveys will start in the next few years. Through 40 narrow-band filters, e.g., the Physics of the Accelerating Universe (PAU) survey will achieve a high accuracy (0.3 per cent) photo-z for $i_{\rm AB} \sim 23$ (Martí et al. 2014). The PAUcam in addition contains u, g, r, i, z filters, so the survey provides a deep photometric ($i_{\rm AB} < 24.1$) over the same area.

How do overlapping photometric and spectroscopic surveys change the constraints on dark energy and modified gravity? A photometric survey with imaging is ideal for WL, while RSD and BAO benefit from the accurate spectroscopic redshifts. Combining the spectroscopic and photometric surveys brings additional

★ E-mail: marberi@strw.leidenuniv.nl (ME); gazta@ieec.uab.es (EG)

benefit. Two overlapping surveys allow cross-correlation of data, e.g. the foreground spectroscopic galaxies with the background shear. Further, the overdensities in both surveys trace the same underlying matter which allows for sample variance cancellations.

Several groups (Bernstein & Cai 2011; Cai & Bernstein 2012; Gaztañaga et al. 2012; de Putter, Doré & Takada 2013; Font-Ribera et al. 2013; Kirk et al. 2013), including the authors, have investigated the effect of overlapping galaxy surveys and found different results for the benefits. This paper follows up our previous paper (Gaztañaga et al. 2012), where we studied overlapping galaxy surveys by combining a 3D $P(k)$ for spectroscopic surveys and 2D C_l estimators for photometric surveys. When doing this, there is a risk of overcounting overlapping modes and not including the full covariance between them. Here, to simplify the combination and to avoid assuming a cosmology, both surveys are analysed using the same angular cross-correlations. In this respect, our approach is similar to that in Asorey et al. (2012) and Kirk et al. (2013), but including all the elements in Gaztañaga et al. (2012). The redshift bin projection in angular correlation removes some radial information within the bin. However, Asorey et al. (2012) showed that angular cross-correlations in narrow bins recover the bulk of the available information.

Section 3 discusses the numerical implementation of the equations for evaluating the angular correlations. The computational time is especially important for parameter constraints, which often require 10^5 to 10^6 sample points in the parameter space. Including the RSD and lensing for many thin redshift bins is computationally challenging, especially when also including multiple galaxy populations, different measurements and finally the cross-correlations between all of them. Further Section 3.7 discusses partial calculations as a method for evaluating the results.

In Section 4, we study the effect of Limber approximation, BAO, RSD and the redshift bin width on the auto- and cross-correlations. Analysing the spectroscopic sample requires narrow redshift bins to capture the radial information. The redshift bin thickness has a large impact on RSD and BAO for both the auto- and cross-correlations. Understanding these is essential to interpret the forecast in the following papers in this series. Especially, we note that the BAO signal is stronger in the cross-correlations between redshift bins than in the auto-correlations. The last subsection focuses on the expected error bars.

This paper is the first in a three-part series. In this paper, we study the modelling of the correlations function. The second paper forecasts the dark energy and growth constraints for galaxy clustering, RSD and WL. In the third paper, we investigate the dependence on bias assumptions. A separate paper compares the constraints for overlapping and non-overlapping photometric and spectroscopic surveys.

2 ANGULAR CORRELATION FUNCTION

2.1 Angular correlation in Fourier space

The observables considered here are fluctuations in galaxy number counts $\delta_{\rm g}$ and galaxy shapes (or ellipticity) δ_γ. These fluctuations are subject to intrinsic large-scale structure (or intrinsic alignments), RSD and WL

$$\delta = \delta^{\rm I} + \delta^{\rm RSD} + \delta^{\rm WL}. \tag{1}$$

Calculation of the intrinsic correlations and the contribution of RSD is described for example in Padmanabhan et al. (2007). Following the notation of Crocce, Cabré & Gaztañaga (2011), the angular correlation in Fourier space can be calculated by

$$C_l = \frac{1}{2\pi^2}\int 4\pi k^2 {\rm d}k\; P(k)\; \psi_l^2(k). \tag{2}$$

For the intrinsic component of galaxy number counts, the kernel $\psi_l(k)$ is

$$\psi_l(k) = \int {\rm d}z\; \phi(z)\; D(z)\; b(z,k)\; j_l(kr(z)). \tag{3}$$

Here $P(k)$ is the power spectrum of the underlying dark matter distribution, $\phi(z)$ is the galaxy selection function (normalized galaxy redshift distribution in our sample), $D(z)$ is the linear growth of structure and j_l is the spherical Bessel function. Galaxy overdensities are related to the matter overdensities through the relation

$$\delta_{\rm g}(z,k) = D(z)\; b(z,k)\; \delta_{\rm m}(z=0,k), \tag{4}$$

where $\delta_{\rm g}$ and $\delta_{\rm m}$ are the galaxy and matter overdensities. Therefore, the power spectrum $P(k)$ can be expressed as $P(k) = D^2 b^2 P_{\rm m}(k)$. The bias ($b$) relates the galaxy and matter overdensities, with details being discussed in Paper III.

Including RSD adds an additional contribution

$$\psi_l(k) = \psi_l(k)^{\rm Real} + \psi_l(k)^{\rm RSD} \tag{5}$$

to the real space contribution (Fisher, Scharf & Lahav 1994; Fisher et al. 1995; Taylor & Heavens 1995). The RSD term in linear theory is given by Kaiser (1987) and Hamilton (1998):

$$\begin{aligned}
\psi_l^{\rm RSD} &= \int {\rm d}z\; f(z)\; \phi(z)\; D(z) \\
&\quad \times [L_0(l)\; j_l(kr) + L_1(l)\; j_{l-2}(kr) + L_2(l)\; j_{l-2}(kr)] \\
L_0(l) &\equiv \frac{(2l^2+2l-1)}{(2l+3)(2l-1)} \\
L_1(l) &\equiv -\frac{l(l-1)}{(2l-1)(2l+1)} \\
L_2(l) &\equiv -\frac{(l+1)(l+2)}{(2l+1)(2l+3)},
\end{aligned} \tag{6}$$

where $f(z)$ is the growth rate, which we write as $f(z) \equiv \Omega_{\rm m}(z)^\gamma$. Note that we assumed that velocities are the same for the galaxies as for matter, so there is no bias term in the RSD contribution.

Weak gravitational lensing changed the galaxy ellipticities and the number densities through magnification effects. Both of these can be described by the convergence field κ. The convergence in a redshift bin j caused by dark matter lenses at z is (Bartelmann & Schneider 2001)

$$p_{\kappa_j}(z) \equiv \frac{3\Omega_{\rm m0} H_0 r(z)}{2H(z)a(z)r_0}\int_z^\infty {\rm d}z' \frac{r(z';z)}{r(z')}\phi(z'), \tag{7}$$

where $\Omega_{\rm m0}$ and H_0 are the matter density and Hubble distance at $z=0$. The quantity $r(z';z)$ is the angular diameter distance between z' and z. In order to estimate the lensing power spectrum, we can use equation (2) and to evaluate the lensing kernel we need to replace $\phi(z)$ by $p_{k_j}(z)$ in equation (3) (with $b=1$), i.e.

$$\psi_l(k) = \int {\rm d}z\; p_{\kappa_j}(z)\; D(z)\; j_l(kr(z)). \tag{8}$$

Gravitational lensing changes the observed number counts through two effects. A galaxy observed close to a foreground matter overdensity will appear brighter, which changes the number of galaxies entering a magnitude-limited sample. This change depends

on the slope of the number counts (s_n). WL magnification also affects the area. The observed area in the background of a matter overdensity will appear larger and would reduce the galaxy density for a fixed number of galaxies. Combining these two effects, the change in δ_g from weak lensing magnification is given by

$$\delta_g^{WL} \propto 5s_n(z_i) - 2, \tag{9}$$

where the slope of the number counts s_n comes from

$$s_n(z_i) \equiv \frac{\mathrm{d}\log_{10} N_n(<m, z_i)}{\mathrm{d}m} \tag{10}$$

and $N_n(<m, z_i)$ is the number of galaxies at redshift z_i with apparent magnitudes less than m. Therefore, the lensing component of galaxy number count fluctuations in equation (1) is

$$\delta_g^{WL} \approx (5s - 2)\delta_\kappa \equiv \alpha\delta_\kappa, \tag{11}$$

where the last equivalence defines α. For simplicity, the galaxy ellipticity γ is assumed here to be directly proportional to κ ($\delta_\gamma^{WL} = 2\delta_\kappa$), but we could in principle easily include additive and multiplicative observational biases in the calculation.

2.2 The Limber approximation

Two approximations greatly simplify the evaluation of the analytic correlation functions. The first one is the narrow-bin approximation, assuming no redshift evolution within a redshift bin. For narrow bins, it can be a good approximation. Second is the Limber approximation; using the relation (Limber 1954; Loverde & Afshordi 2008; Jeong, Komatsu & Jain 2009)

$$\frac{2}{\pi}\int k^2\mathrm{d}k\; j_l(kr)\; j(kr') = \frac{\delta^D(r - r')}{r^2} \tag{12}$$

can remove one additional integration. The symbols r and r' are the distances to the two redshifts to correlate. In the case of $r \neq r'$, which is the case for cross-correlations between redshift bins, the contribution is zero for the Limber approximation. Later we will compare the exact calculations and the Limber approximation in detail.

In the notation $C_{A_iB_j}$ then A and B are the observables, i.e. galaxies (g) or shear (γ). An additional letter behind g (e.g. gF) indicates a specific galaxy population. The indices i and j denote the redshift bin and $i = j$ is the auto-correlation, while $i \neq j$ is a cross-correlation. Below follows a short summary of the formula given in Gaztañaga et al. (2012). To simplify the notation, we define

$$\mathcal{P}(k, z) \equiv \frac{P(k, z)}{r_H(z)r^2(z)}, \tag{13}$$

where $\mathcal{P}(k, z)$ is the power spectrum and $r_H(z) \equiv \partial r(z)/\partial z$. The galaxy clustering can then be written as

$$C_{gn_igm_j} \approx \left[b_{n_i}b_{m_j}\frac{\delta_{ij}^K}{\Delta_i} + \alpha_{m_j}b_{n_i}p_{ij}\right]\mathcal{P}_i + \alpha_{n_i}\alpha_{m_j}C_{\kappa_i\kappa_j}(l), \tag{14}$$

where b are the galaxy biases and δ_{ij}^K is the Kronecker delta. The second term is the correlation between the intrinsic galaxy lenses and the magnified galaxy counts. This magnification term includes the lensing potential

$$p_{ij} = \frac{3\Omega_{m0}H_0}{2H(z_i)a_i}\frac{r_i r(z_j; z_i)}{r_0 r_j} \tag{15}$$

which is evaluated in the narrow-bin approximation. As before, the $r(z; z')$ notation indicates an angular diameter distance between z and z'. The term Ω_{m0} denotes the matter density at $z = 0$ and $r_0 = c/H_0$. The last term in equation (14) correlates magnified lenses with magnifies sources. In practice, the first two terms dominate.

The galaxy-shear correlation is

$$C_{gn_i\gamma_j} \approx b_{n_i}p_{ij}P_i + 2\alpha_{n_i}C_{\kappa_i\kappa_j} \tag{16}$$

when $z_i < z_j$, otherwise zero. Finally, there is the $C_{\kappa\kappa}$ term,

$$C_{\kappa_i\kappa_j} \approx \int_0^{z_i}\frac{\mathrm{d}z}{r_H}\left(\frac{3\Omega_m H_0}{2Har_0}\right)^2\frac{r(z_i; z)r(z_j; z)}{r_i r_j}\mathcal{P}(k, z) \tag{17}$$

which is proportional to the shear–shear ($C_{\gamma\gamma} = C_{\kappa\kappa}/4$) signal and is also part of the calculations for C_{gg} and $C_{g\kappa}$ in equations (14) and (16). One integration remains, since the lensing is affected by all the matter in front of the redshift bin. Using a thin bin and only integrating over the lens or source bin would lead to wrong results (Gaztañaga et al. 2012). When showing correlation with the Limber approximation, we use the expressions above.

3 ALGORITHM FOR 2D CORRELATIONS

3.1 Motivation

Estimating the angular correlation function involves integrating equation (2) using equations (3) and (6) for the intrinsic and RSD contributions, and then equation (7) to add lensing. For the intrinsic and RSD, the calculations are three-dimensional integrals, two for each of the redshift bins and one over scale. When adding lensing one should, to be correct, use two more integration, corresponding to the dark matter lensing the source and the lens redshift. This section looks at how to collapse the multidimensional integrals into matrix multiplications. It results in an efficient and understandable algorithm.

Next level of complication includes using multiple observations, like galaxy counts and shear, splitting tracers into multiple populations and doing the analysis with a large number of redshift bins. One could approach this problem by constructing a function or equivalent returning the correlation for a given observation, tracer and pair of redshift bins. But this approach is not very efficient. In general, organizing a code introducing additional layers helps the organization, while removing layers improves the speed. Part of this section discusses how to simultaneously calculate the correlations for different tracers, observations and pairs of redshift bins. The idea is to save time by reusing parts of the calculations.

Multiple dimensional integration over spherical Bessel functions is a potential source for numerical errors. Two common approaches for testing the accuracy are to compare against other codes and to increase resolution settings within the code. We have of course tried both. A third approach is to inspect if partial results of the calculations make sense. In Section 3.7 we discuss how this can be done in practice and explore potential problems in the integration.

One alternative to do these calculations is to use publicly available software packages like CAMB (Challinor & Lewis 2011a,b) or CLASS (Blas, Lesgourgues & Tram 2011a,b; Lesgourgues 2011a,b; Lesgourgues & Tram 2011; Tram & Lesgourgues 2013) and its extension: CLASSgal (Di Dio et al. 2013). But these only became available in 2011 after the project had already started. Moreover, integrating the codes to be able to use arbitrary $n(z)$, bias parametrization, different galaxy populations and magnification slopes would itself be a significant addition. We hope the formalism provided here gives another view on how to evaluate the correlations in Fourier space, which is also quite efficient and produces very fast results for a given accuracy. To benchmark the performance, we used the 72-bin spectroscopic population and included both RSD and WL. Running

on a MacBook Air (from 2013), we evaluated the counts–counts, counts–shear and shear–shear correlation for 25 l-values in approximately 10 s. Using CAMB instead of Eisenstein-Hu (EH) will only increase the time for evaluating the power spectrum and not the integration, leading to a moderate increase in runtime.

3.2 Implementation

As detailed in Section 2, the starting point is that the fluctuations, in both galaxy counts δ_g and galaxy shear δ_γ, are made up of three contributions: intrinsic, redshift space and lensing:

$$\delta_A(k,z) = \delta_A^{\rm I}(k,z) + \delta_A^{\rm RSD}(k,z) + \delta_A^{\rm WL}(k,z), \tag{18}$$

where A can be one of the two probes: $A = g$ for galaxy counts or $A = \gamma$ for shear ellipticity in galaxies. When correlating these overdensities in two redshift bins labelled i and j:

$$C_{ij}(l) = \int {\rm d}k \int_{{\rm Bin}\,i} {\rm d}z_i \int_{{\rm Bin}\,j} {\rm d}z_j \left\langle \delta(k,z_i), \delta(k,z_j) \right\rangle . \tag{19}$$

Thus, the final correlation includes nine different terms for each probe or cross-combination (i.e. $\delta_g\delta_g$, $\delta_\gamma\delta_\gamma$ and $\delta_g\delta_\gamma$), which are not all equally important. For the time being, all the effects will be included in the calculation without further approximation. Following this general approach leads to a simple implementation with a good performance.

3.3 Tomographic integration

Numerical deterministic integration of a function f over a finite interval can be expressed as[1]

$$\int {\rm d}y\ f(y) = \sum_x w_x f(y_x), \tag{20}$$

where w_i is a set of weights and y_i is a set of sample points, which differs between algorithms. Adaptive algorithms are often on the form above and then subdividing the integral domain where the required accuracy has not been achieved.

Ignoring multiple tracers and different probes by now, the integration to evaluate the C_l can be written as

$$C_{ij}(l) = \int {\rm d}k\ G_i(k)\, G_j(k) \equiv \sum_x\ w_x\ G_i(k_x)\, G_j(k_x), \tag{21}$$

where the form of $G(k)$ follows from equation (2) and i and j denote two redshift bins. One could evaluate the integral (21) for each pair (i, j) of redshift bins. Alternatively by defining

$$H_{sx} \equiv \sqrt{w_x}\ G_s(k_x) \tag{22}$$

the integration (21) can be rewritten in terms of equation (22) as

$$C_{ij}(l) = \sum_x H_{ix} H_{jx}. \tag{23}$$

In this form, the matrix $\mathbf{H}$ can be constructed once and then used to compute the correlations between all bins. More importantly, the form (23) is closely related to the matrix product. If we consider $\mathbf{C}$ to be a matrix where C_{ij} is the correlation between bin i and j, the whole $\mathbf{C}$ can be calculated as

$$\mathbf{C} = \mathbf{H}\mathbf{H}^{\rm T} \tag{24}$$

where 'T' denotes the transpose. The calculations are normally expressed as loops over i, j and k. Expressing the operations as matrix multiplication makes it possible to evaluate the expression using DGEMM from level-3 BLAS.[2] This is particularly important in higher level languages, like PYTHON, where looping is very slow. Also FORTRAN, C and C++ should benefit since DGEMM has highly efficient implementations like MKL from Intel and the open source OpenBlas. In addition, the expressions look readable and require less lines of code.

One suitable algorithm for evaluating oscillating integrands is the Clenshaw–Curtis (CC) quadrature. Appendix B includes a brief introduction and how to handle changes of integral domain for the tomographic integration and here we include the explicit integration formulas.

Using the CC algorithm, one needs to split equation (24) into two parts:

$$\mathbf{C} = \mathbf{H}^+(\mathbf{H}^+)^{\rm T} + \mathbf{H}^-(\mathbf{H}^-)^{\rm T} \tag{25}$$

where

$$H^+_{sx} = \sqrt{k_w \mathcal{W}_x} G_s \left(\bar{k} + k_w \cos\frac{n\pi}{n}\right) \tag{26}$$

$$H^-_{sx} = \sqrt{k_w \mathcal{W}_x} G_s \left(\bar{k} - k_w \cos\frac{n\pi}{n}\right) \tag{27}$$

$$\bar{k} = \frac{1}{2}(k_{\rm min} + k_{\rm max}) \tag{28}$$

$$k_w = \frac{1}{2}(k_{\rm max} - k_{\rm min}) \tag{29}$$

and the weights $\mathcal{W}$ are given in Appendix B.

3.4 Intrinsic correlations and RSD

This subsection focuses on the expression for G in equation (21), taking into account the intrinsic correlation and RSD contribution, while the next subsection explains the lensing contribution.

The integration over the redshift binning can be done through the following relations:

$$G_i^{\rm I} = \tilde{G} \int_{{\rm Bin}i} {\rm d}z \psi^{\rm I}(z,k) \tag{30}$$

$$G_i^{\rm RSD} = \tilde{G} \int_{{\rm Bin}i} {\rm d}z \psi^{\rm RSD}(z,k) \tag{31}$$

$$\tilde{G} = \frac{2}{\pi} k \sqrt{P(k)} \tag{32}$$

using equations (2), (3) and (6). As stated earlier, the goal is to express the integration through matrix multiplication. First, the redshift range where some bin has support is divided into a grid. For narrow top-hat bins, one can simply use the bins themselves. The function $\phi_i(z)$ in equation (3) denotes the probability of a galaxy in bin i having true redshift z. In photometric surveys, the bins are not top-hat, but are for each bin given by a probability distribution. The probability is found by binning in photometric redshift and the comparing with the spec-z in the calibration sample.

[1] Integration algorithms can also be stochastic. For one example in astronomy, MPTBreeze uses the Vegas algorithm to efficiently evaluate the two-loop propagator (Crocce, Scoccimarro & Bernardeau 2012). Further, some integration algorithms use knowledge of the function derivatives.

[2] http://www.netlib.org/blas/

The probability distributions are then combined into one matrix

$$\phi \equiv \begin{pmatrix} \phi_{00} & \phi_{01} & \dots & \phi_{0n} \\ \phi_{10} & \phi_{11} & \dots & \phi_{1n} \\ \dots & \dots & \dots & \dots \\ \phi_{n0} & \phi_{n1} & \dots & \phi_{nn} \end{pmatrix}, \tag{33}$$

where ϕ_{ij} is the part of ϕ_i overlapping with the underlying grid bin j. In the case of narrow non-overlapping redshift bins using the bins itself as a grid, then $\phi_{ij} = \delta_{ij}\phi_{ij}$. Integration in redshift is also done using the CC algorithm inside each of the redshift grid bins. The evaluation points in redshift, using N_z integration points inside grid bin j, are

$$z_{jx}^{+} \equiv \bar{z}_j + z_j^w \cos\frac{n\pi}{N_z} \tag{34}$$

$$z_{jx}^{-} \equiv \bar{z}_j - z_j^w \cos\frac{n\pi}{N_z} \tag{35}$$

$$\bar{z}_j \equiv \frac{1}{2}\left(z_j^{\rm Min} + z_j^{\rm Max}\right) \tag{36}$$

$$z_j^w \equiv \frac{1}{2}\left(z_j^{\rm Max} + z_j^{\rm Min}\right) \tag{37}$$

with z_j^{+} and z_{jx}^{-} denoting the contribution to the integral over bin j. In practice, one concatenates the two 1D arrays z_j^{+} and z_{jx}^{-} into a larger array before evaluating the probability functions.

One also needs weights for integrating over the redshift bins. The weight arrays $w_i, \dots, w_{ngrid}$ for each of the *ngrid* redshift grid bins are then concatenated into the array

$$\mathcal{W}_z \equiv [w_0, w_1, \dots, w_{ngrid}]. \tag{38}$$

If one uses the same number of integration points in each bin, as we do, then the operation reduces to repeating the same weight matrix *ngrid* times. The probability functions (33) and (38) can then be combined into

$$(W^{\rm Gal})_{ij} = \phi\ \mathcal{W}_z \tag{39}$$

where the multiplication is with the second index in ϕ. Integration over redshift bins in equations (31) and (32) can, dropping the superscript, be written as

$$G = \phi\ y(z, k), \tag{40}$$

where the z binning is the one used for the redshift grid when evaluating ϕ. The function $y(z, k)$ is defined through $\psi(z, k) = \phi(z, k)y(z, y)$, and can explicitly be written as

$$y^{\rm I}(z, k) = \tilde{G}(k)\ D(z)\ b(z, k)\ j_l(kr(z)). \tag{41}$$

In the case of RSD, one should add a similar term

$$y^{\rm RSD}(z, k) = \tilde{G}(k)\ f(z)\ D(z)\ [L_0(l) j_l(kr) + L_1(l)\ j_{l-2}(kr) + L_2(l)\ j_{l-2}(kr)], \tag{42}$$

where $L_0(l)$, $L_1(l)$ and $L_2(l)$ are defined as in equation (6). To implement this, one can construct splines of the spherical Bessel functions. Instead of evaluating j_l, j_{l-2} and j_{l+2}, the linear combination used in equation (42) is calculated once and then stored in splines.

3.5 Weak gravitational lensing

Weak gravitational lensing affects the galaxy shapes and counts at the source redshift from the foreground matter, while the intrinsic correlations and RSD contributions are caused by the matter overdensities at the same redshift. In addition to integration over the scale and the two redshift bins, evaluating the lensing contribution requires integrating over the foreground dark matter. While five-dimensional integrals sound tricky, they can be evaluated efficiently by reusing terms and considering the correlations between all redshift bins at once.

To include the lensing effect described in equation (7), we use

$$\eta(z_j, z_i) \equiv \frac{3\Omega_{\rm m0} H_0 r(z)}{2H(z)a(z)r_0}\frac{r(z'; z)}{r(z')}, \tag{43}$$

where z_i is the lens and z_j the source redshift. Defining the second index for the lens redshift allows to add lensing later using left multiplication. The lensing contribution is then

$$G^{\rm WL} \equiv (\phi\mathcal{W}_z)\ (\tilde{\eta}\mathcal{W}_z)\ y^{\rm Mat} \tag{44}$$

$$y^{\rm Mat}(z, k) \equiv \tilde{G}\ D(z)\ j_l(kr(z)), \tag{45}$$

where $\tilde{\eta}(z_j, z_i) \equiv \alpha(z_j)\eta(z_j, z_i)$ either includes the magnification factor for galaxy counts or is set to unity for cosmic shear. When evaluating η, one uses the same redshift binning as ϕ. In this notation, the same ϕ is also used for the intrinsic correlations and RSD. The disadvantage is that we need to use the highest redshift resolution required. However, this allows us to reuse e.g. the evaluated spherical Bessel functions j_l, for all contributions to the overdensities.

3.6 Combining multiple terms

In the previous subsections, the focus was an efficient evaluation of the cross-correlations including the intrinsic correlation, RSD and WL. These contributions were included in the terms $G^{\rm I}$, $G^{\rm RSD}$ and $G^{\rm WL}$ and to account for all effects we just have to sum them

$$G = G^{\rm I} + G^{\rm RSD} + G^{\rm WL} \tag{46}$$

and calculate the C_l (equation 24). These calculations alone could require seven nested loops, if implemented in a straightforward and naive approach. In addition, a forecast or Markov Chain Monte Carlo (MCMC) run requires the following layers:

(i) cosmological parameters,
(ii) l-value,
(iii) galaxy population in bin 1,
(iv) galaxy population in bin 2,
(v) observable in bin 1 and
(vi) observable in bin 2.

The efficiency of the integration depends on the matrix order. Matrix multiplication is an associative operation, i.e.

$$\mathbf{A}\,(\mathbf{BC}) = (\mathbf{AB})\mathbf{C}, \tag{47}$$

where $\mathbf{A}$, $\mathbf{B}$ and $\mathbf{C}$ are matrices. In terms of implementation, the order affects the number of the operations. Assume that the matrix dimensions are

$$\mathbf{A} = k \times m \tag{48}$$

$$\mathbf{B} = m \times n \tag{49}$$

$$\mathbf{C} = n \times s. \tag{50}$$

Evaluating $\mathbf{A}(\mathbf{BC})$ requires $mns + kms$ operations, while evaluating $(\mathbf{AB})\mathbf{C}$ requires $kmn + kns$ operations. Depending on the k, m, n values, one ordering is the most efficient. For the accuracy used in

our implementation, we calculated the number of operations needed for different orders of integrating using the default resolution in redshift, scale and around 100 redshift bins. The most efficient choice was first integrating out lensing, then binning in redshift and finally integrating over the scale. This order was in the previous subsections reflected both in the formulas and in the presentation.

3.7 Investigating partial calculations

The previous subsections described an algorithm for calculating the 2D correlations in Fourier space including the intrinsic correlation, RSD and lensing. In addition to comparing the resulting C_l with the public software, one can directly check steps of the calculations. The algorithm first integrates over all redshift variables and then over the scale. In the notation of equation (24), one can construct a cumulative sum

$$C_{ij}^{\rm Partial}(k_{\rm c}) = \sum_{x}^{k(x)<k_{\rm c}} H_{ix} H_{xj} \tag{51}$$

of the correlations, where $k(x) < k_{\rm c}$ means the sum of indices x until the one corresponding to $k_{\rm c}$. Note that the $k_{\rm c}$ used in equation (51) is only defined to see which scales contribute to a correlation and is not the maximum k considered in the forecast.

In the case of insufficient integral precision in redshift, the numerical artefacts often enter at high k due to the product $kr(z)$ in $\psi_l(k)$ (equation 3). These errors can create serious problems for Fisher matrices, where high precision is needed, and are easily detectable looking at $C^{\rm Partial}$, but difficult to spot looking at the final correlations.

In the remainder of this subsection, we present figures of $C^{\rm partial}$ for counts–counts auto- and cross-correlations, and counts–shear, shear–shear auto-correlations. These figures are not only useful for detecting errors, but also help to understand which scales contribute to the correlations. The fiducial cosmological model used is Λ cold dark matter with $\Omega_{\rm m} = 0.25$, $\Omega_{\rm b} = 0.044$, $\Omega_{\rm DE} = 0.75$, $h = 0.7$, $w_0 = -1$, $w_a = 0$, $n_s = 0.95$ and $\sigma_8 = 0.8$ corresponding to the values used in the MICE simulations (Fosalba et al. 2008; Crocce et al. 2010). Galaxies are biased through the relation $b(z) = 2 + 2(z - 0.5)$, except for the thick redshift bins in Fig. 5 which has a galaxy bias of $b(z) = 1.2 + 0.4(z - 0.5)$. These bias values are chosen to exactly match the bright and faint population introduced in Eriksen & Gaztañaga (2015, hereafter Paper II). The power spectrum used is EH (Eisenstein & Hu 1998). Using a numerical Boltzmann code for the power spectrum instead does not introduce significant changes in our conclusions, but is somehow similar to a minor shift in some of the fiducial cosmological parameters.

Fig. 1 includes four $C^{\rm Partial}$ lines for the auto-correlations at $l = 256$ of galaxy counts in four narrow redshift bins. These auto-correlations include RSD and a sub-dominant magnification term. From the Limber approximation, one expects the largest contribution from $k = (l + 1/2)/\chi(z_{\rm m})$, where $\chi(z_{\rm m})$ is the mean comoving distance of the redshift bin. For the fiducial cosmology, one expects the main contribution to the correlations around $k = 0.40$, 0.26, 0.15, 0.11 Mpc h^{-1} for the redshift bins $z = 0.23$, 0.35, 0.65, 1.01 as shown by the vertical lines in Fig. 1. The estimated scale for the main contribution to the correlation agrees well with the figure.

In Fig. 2, four thin redshift bins are cross-correlated with the adjacent redshift bin. Each cross-correlation in the figure corresponds to one auto-correlation in Fig. 1. Comparing the two figures, similar scales contribute to both the auto- and cross-correlations. A characteristic feature of the cross-correlation is the sharp peak.

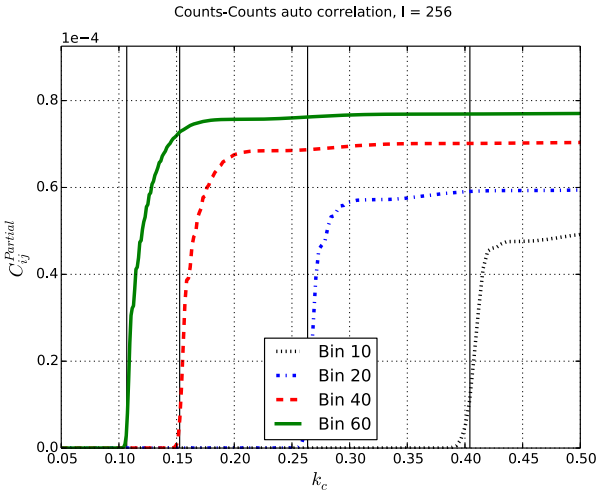

Figure 1. Cumulative contribution to counts–counts auto-correlations at $l = 256$ from different scales ($C^{\rm Partial}$). The correlations include k-values until the limit displayed on the x-axis. Lines in the figure correspond to the redshift bins $0.22 < z_{10} < 0.23$, $0.34 < z_{20} < 0.36$, $0.64 < z_{40} < 0.65$ and $1.00 < z_{60} < 1.02$.

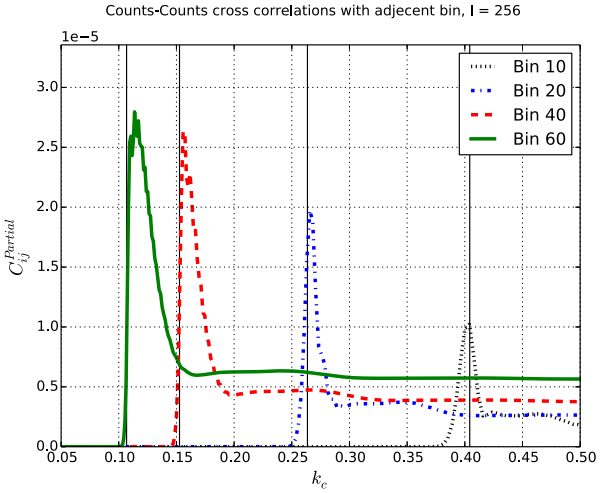

Figure 2. Cumulative contribution to counts–counts cross-correlations at $l = 256$ from different scales ($C^{\rm Partial}$). The correlations include k-values until the limit displayed on the x-axis. The first correlation is between $0.22 < z_{10} < 0.23$ and $0.23 < z_{11} < 0.24$, the second between $0.34 < z_{20} < 0.36$ and $0.36 < z_{21} < 0.37$, the third between $0.64 < z_{40} < 0.65$ and $0.65 < z_{41} < 0.67$, and the fourth between $1.00 < z_{60} < 1.02$ and $1.02 < z_{61} < 1.04$.

An auto-correlation has only positive contribution as a function of scale, while for a cross-correlation the spherical Bessel functions are slightly out of phase. This results in k values with negative contributions and results in a filtering of small scales (see Section 4.2.2).

Fig. 3 cross-correlates overdensities of foreground galaxies with background shear. All lines use the source redshift bin $1.16 < z < 1.19$, while the number of foreground redshift bins equals those in the previous two figures (Figs 1 and 2). The scales contributing to the counts–shear cross-correlation are precisely the ones contributing to the auto-correlation. That is expected from looking at the Limber equations for counts–counts (equation 14) and counts–shear (equation 16), both including the power spectrum evaluated at $k = (l + 0.5)/\chi(z_{\rm m})$. Further, in the auto-correlation the amplitude increases with redshift because galaxy bias increases

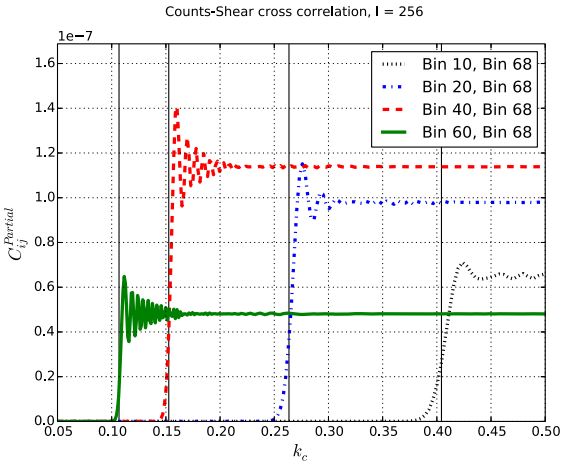

Figure 3. Cumulative contribution to counts–shear cross-correlations at $l = 256$ from different scales ($C^{\rm Partial}$). The correlations include k-values until the limit displayed on the x-axis. For all the correlations, the background is $1.16 < z_{68} < 1.19$, while the foreground redshift bins are $0.22 < z_{10} < 0.23$, $0.34 < z_{20} < 0.36$, $0.64 < z_{40} < 0.65$ and $1.00 < z_{60} < 1.02$.

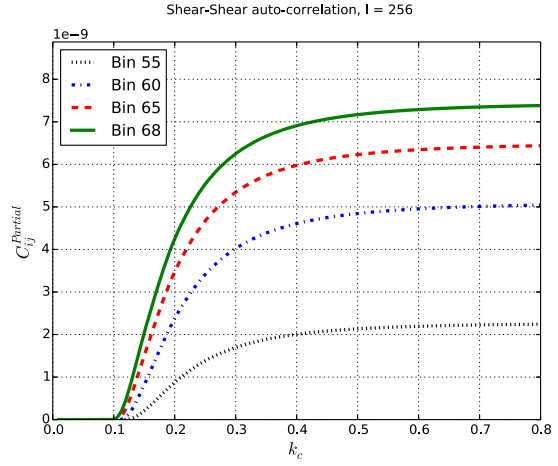

Figure 4. Cumulative contribution to shear–shear auto-correlations at $l = 256$ from different scales ($C^{\rm Partial}$). The correlations include k-values until the limit displayed on the x-axis. Lines correspond to the following thin redshift bins: $0.90 < z_{55} < 0.92$, $1.00 < z_{60} < 1.02$, $1.10 < z_{65} < 1.12$ and $1.16 < z_{68} < 1.19$.

with redshift. For counts–shear the correlation peaks with redshift and is lower for the highest redshift bin. This effect comes from the lensing efficiency (equation 15), which has a similar peak in redshift. One can also see oscillations around the peak in k. These oscillations come from the galaxy counts being negatively correlated with a redshift range of nearby matter which again lenses the background shear.

Fig. 4 is the shear–shear auto-correlation for four redshift bins. These redshift bins differ from the previous figures (Figs 1 and 2) since the lensing signal is stronger for higher redshift. The signal results from a range of scales because the lensing kernel is broad and the shear–shear correlations convolve two lensing kernels. This is in contrast to the counts–counts and counts–shear which peak around a specific scale. Even if the lensing kernel is broad, correlating with a narrow foreground redshift bin results in a contribution from a narrow range of scales. Therefore, one often describes the shear–shear as a 2D signal, while counts–counts and counts–shear being 3D.

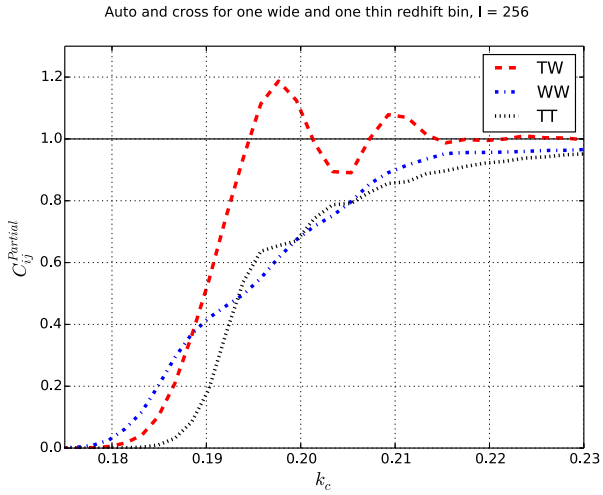

Figure 5. Cumulative contribution for different scales. Auto-correlations and the cross-correlations for two overlapping thin and thick redshift bins. The thin redshift bin (label T) $0.497 < z < 0.512$ and the thick one (label W) $0.44 < z < 0.54$. These bins are selected to include $z = 0.5$ and the thick bin is 6.7 times wider than the thin redshift bin. To show all three lines together, they are normalized to 1 at the asymptotic value and the scale range is limited.

Fig. 5 includes the count–count auto-correlation for a thin and a thick overlapping redshift bin, together with their cross-correlation. As expected, the thick redshift bin has contributions from a wider range of scales. For a decreasing redshift bin width, the correlations do not approach a delta function in scale. Further, as seen in the decline of $C^{\rm Partial}$, cross-correlations of overlapping redshift bins have both positive and negative contributions. One can understand the effect by decomposing the cross-correlation into the overlapping and non-overlapping regions in redshift. For the overlapping part, the cross-correlation behaves similar to the auto-correlation in Fig. 1, while the non-overlapping parts are like the cross-correlations between adjacent bins in Fig. 2. The cross-correlation of overlapping bins combines these contributions, but is closer to the auto-correlation which has the strongest signal.

3.8 Converting C_l to $w(\theta)$

So far, this paper has expressed the correlations in Fourier space. Equivalently, they could be defined and calculated in $w(\theta)$, which is the 2D correlation function in configuration space. Converting from C_l to $w(\theta)$ is a linear combination (Dodelson 2003)

$$w(\theta) = \sum_l \frac{2l+1}{4\pi} C(l) L_l(\cos\theta), \tag{52}$$

where L_l is the Legendre polynomial of order l. The sum is theoretically infinite, while in practice one sums until the result converges. In this subsection, we explicitly show how to convert from C_l to $w(\theta)$ using matrix multiplication, to convert multiple correlations in one multiplication. This is afterwards extended to also efficiently integrate the angular bins in one multiplication.

Let C_{xl} be the 2D correlations in Fourier space stored with the first (x) and second (l) index, respectively, being the observable and the l-value. Conversion from C_l to $w(\theta)$ is done through the matrix multiplication

$$w_{xi} = \sum_l C_{xl} S_{li}, \tag{53}$$

where S is defined by

$$S_{li} \equiv \frac{2l+1}{4\pi} L_l(\cos\theta_i) \tag{54}$$

with θ_i being the mean of angular bin i. The angular bin has a thickness; therefore, the correct solution is

$$w[\theta_A, \theta_B] = \frac{1}{\theta_B - \theta_A} \int_{\theta_A}^{\theta_B} \mathrm{d}\theta\, w(\theta) \tag{55}$$

when considering $w(\theta)$ in an angular bin $[\theta_A, \theta_B]$. When using a linear binning in angle, this effect can often be neglected, but results in problems at large angles if using logarithmic spacing in angle and too few bins. The formulas for the integration below use the CC algorithm.

To integrate over angular bins, we first define

$$k_m \equiv \cos\left(\frac{m\pi}{N_{\mathrm{wbin}}}\right) \tag{56}$$

$$x^{\pm}[\theta_A, \theta_B]_n \equiv \theta_B + \frac{1}{2}(\pm k_m - 1)(\theta_B - \theta_A), \tag{57}$$

where N_{wbin} is the number of integration points inside each angle bin. The expressions $x^{\pm}$ are the integral points for the two contributions to the integration over an angular bin $[\theta_A, \theta_B]$. If A and B denote the edges of the angular bins and n the number of angular bins, then

$$\theta^{\mathrm{Int}} \equiv \left(x^-[\theta_0, \theta_1] \mid x^+[\theta_0, \theta_1] \mid \cdots \mid x^-[\theta_{\mathrm{n}}, \theta_{\mathrm{n+1}}] \mid x^+[\theta_{\mathrm{n}}, \theta_{\mathrm{n+1}}]\right) \tag{58}$$

gives a vector with all intermediate angles in the integration for all angular bins. The integration weights is combined in

$$\phi^{\mathrm{Int}} \equiv \begin{pmatrix} w & w & & & & & \\ & & w & w & & & \\ \cdots & & \cdots & & \cdots & & \cdots \\ & & & & & w & w \end{pmatrix} \tag{59}$$

where the non-included entries are zero and the matrix is block diagonal. Conversion from C_l to $w(\theta)$, also integrating over angle, is done using

$$S' \equiv S(\phi^{\mathrm{Int}})^{\mathrm{T}} \tag{60}$$

$$w = C_l^{\mathrm{T}} S'. \tag{61}$$

One could instead use a simpler algorithm leading to less complicated formulas. A key to implementing these formulas is using a mathematical library or language with user-friendly array calculations. For example, with Numpy (PYTHON library), equation (59) can be reduced to a one-line expression. Constructing s' is compared to calculating the correlations very fast. In addition, these formulas require estimating S' only once for one specific angular bin and maximum summation value in l. When estimating a Fisher matrix or running an MCMC chain, these matrices only need to be computed once.

4 IMPACT OF LIMBER, RSD AND BAO

First we quantify the importance of using the exact integrals instead of the Limber approximation. Then we study in detail the effects of RSD and BAO on the auto-correlations and cross-correlations. In particular because the importance of these effects depends strongly on the redshift bin width. Since a 2D analysis is most widely applied to photometric surveys in broad redshift bins (i.e. $\Delta z \approx 0.1$), it is important to investigate here the effect for the narrower redshift bins ($\Delta z = 0.01$) that we are proposing to constrain cosmological models including the effects of BAO and RSD in Paper II. Galaxies are biased through the relation $b(z) = 2 + 2(z - 0.5)$, except for the fixed bin in Fig. A2.

The first and second subsections focus, respectively, on the auto- and cross-correlations. For many of the figures, the same correlations are presented both in Fourier space (C_l) and configuration space $w(\theta)$. C_l plots are directly related to the formalism presented in Section 2, but the effect of e.g. BAO is easier to understand using $w(\theta)$. For forecasts the C_l are preferred, since the Gaussian, unmasked and full-sky covariance is block diagonal in l-values. For analysing data, one might prefer $w(\theta)$, since Fourier space correlations can be harder to interpret. Therefore, we include $w(\theta)$ plots to make this section more general than only supporting the forecast.

Signal-to-noise (S/N) and error bars are an essential part of observational physics. Decades of preparation and billions of dollars are spent, taking a narrow perspective, to reduce the error bars on the measured correlations to improve constraints on cosmological parameters. Effects entering in the observables are mostly interesting when being comparable large to the error bars. A naively promising signal might be uninteresting due to low S/N. In the last subsection we study the S/N and the errors on the correlations.

A special case is cross-correlations between partially overlapping bins, which have traits of both auto- and cross-correlations. These and the non-linear effects are studied in Appendix A.

4.1 Auto-correlations

4.1.1 Comparing effects as a function of bin width

Fig. 6 shows the C_l and $w(\theta)$ auto-correlations for different bin width Δz. We can see how the amplitude of the overall correlations and the contrast of the BAO wiggle in C_l or BAO peak in $w(\theta)$ decreases as we increase Δz.

The continuous line in Fig. 7 shows the ratio of the Limber approximation to the exact calculation (both without RSD) for C_l, with the top and bottom panels, respectively, using a narrow ($\Delta z = 0.01$) and wide ($\Delta z = 0.1$) redshift bin. All the correlations are centred around $z = 0.5$. The other lines show the ratio after removing RSD (dashed), BAO (dot–dashed) or both (dotted). For RSD the ratio is below 1, meaning the RSD contribute positively to the correlations. Including the correlations for two bin widths in Fig. 7 shows how the relative size of different effects depends on the redshift bin width.

When comparing the effects in a wide and narrow redshift bin, the largest effect comes from the inaccuracy of the Limber approximation in narrow bins. The Limber approximation is known to break down for thin bins. This can be seen in equation (14), where the division on the redshift bin width would result in infinite correlations for infinitely thin bins. At $l = 150$, the Limber approximations account for 3 per cent for bin width 0.01, which can be tolerated depending on the survey accuracy, while for a narrow redshift bin the effect is close to 50 per cent. This for all purposes is too large.

4.1.2 Limber approximation

The Fig. 8 includes in real space the ratio of the Limber approximation to the exact calculations for both the C_l and $w(\theta)$. From the ratios of the correlations in Fourier space, there is a huge difference in using a wide or a narrow redshift bin. A goal of the forecast in Paper II is to include radial information in the spectroscopic sample.

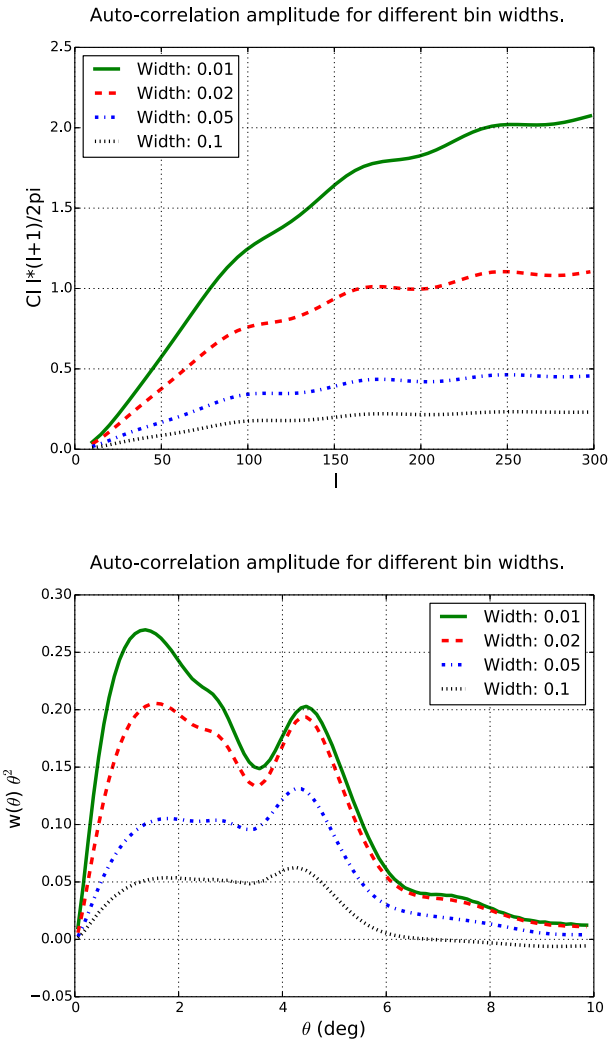

Figure 6. The amplitude of auto-correlations for different redshift bin widths. In both panels, the redshift bin centred in $z = 0.5$, with the four lines corresponding to redshift bin widths $\Delta z = 0.01, 0.02, 0.05, 0.1$. The top and bottom panels correspond, respectively, to C_l and $w(\theta)$, with the y-label indicating prefactors.

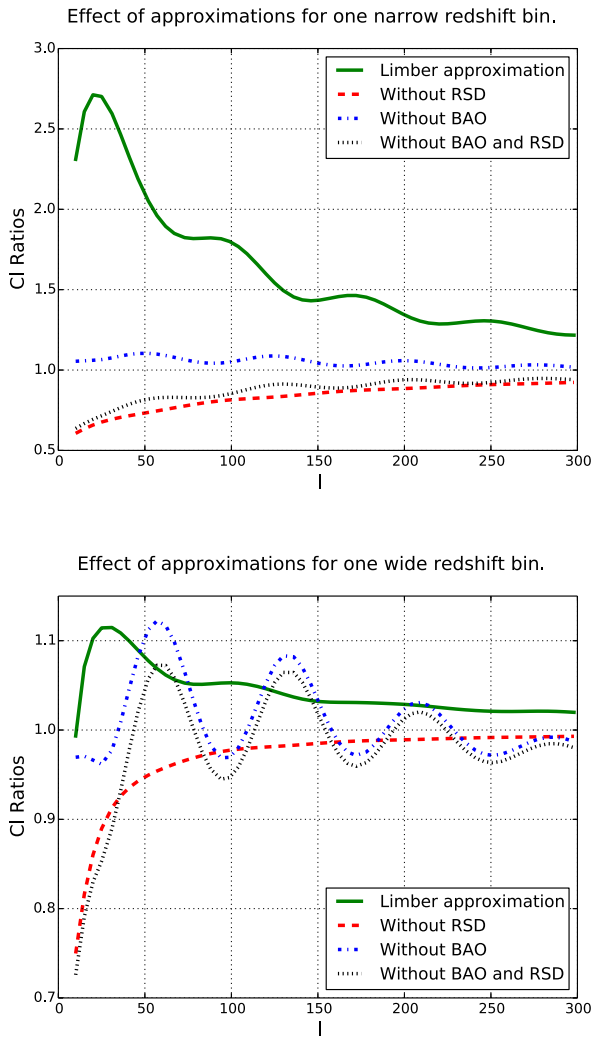

Figure 7. Comparison of the effect of Limber approximations, RSD and BAO. The redshift bin is centred around $z = 0.5$ and width $\Delta z = 0.01$ (top) or $\Delta z = 0.1$ (bottom). Ratios plotted with respect to the exact fiducial calculation (including RSD and BAO), except for the Limber case. Since the Limber approximation is in real space, the ratio is with respect to the real space correlations (i.e. without RSD).

The next subsection shows how cross-correlation between adjacent redshift bins can be used for measuring radial correlation and this requires bins $\Delta z = 0.01(1 + z)$ for our choice of $k_{\rm max}$. From Fig. 8, for our purpose the Limber approximation is unusable even for the auto-correlations.

4.1.3 Redshift space distortions

RSD do not change the angular positions of galaxies, but they do change their angular correlation when selected in observed redshift bins as large-scale motions move structures across the boundaries in a spatially coherent way (see Section 2 and references therein). Fig. 9 shows the redshift-to-real space ratio when varying the redshift bin width. When analysing galaxy clustering in photometric surveys, the standard approach uses 2D correlations in thick redshift bins. A broad-band photo-z scatter rms is around $0.01(1 + z)$ to $0.05(1 + z)$ depending e.g. on the magnitude, filters, exposure times and calibration sample. Because of the photo-z scatter, analysing the data in narrower bins would give little improvements. With narrow bins one would need to model photo-z transitions between redshift bins and their uncertainty (Gaztañaga et al. 2012). For a spectroscopic survey, one can analyse the data in narrow bins.

The effect of RSD results in a significant amplitude increase as shown in Fig. 9. A lower bin width results in a higher amplitude. For low values, $10 < l < 30$, the effect for the broad bin ($\Delta z = 0.1$) is 10–30 per cent, while the effect is 45–50 per cent for the narrow bin ($\Delta z = 0.01$). More importantly, the scales affected depend on the bin width. For the thick redshift (top panel), RSD only contribute significantly for $l < 50$, while for $\Delta z = 0.01$ the effect is still 10 per cent at $l = 300$. Physically, the RSD in the 2D correlations is a boundary effect. When decreasing the bin width, the bulk decrease and the RSD boundary effect become more important. This is why Fig. 9 looks similar to Fig. 8, as the Limber approximation can also be cast as a boundary effect in real space.

In configuration space (Fig. 9, bottom panel), the redshift-to-real space ratio peaks around 3.5 deg, shifting only slightly depending on the bin width. For the thinnest bin ($\Delta z = 0.01$), the RSD/real space ratio nearly doubles compared to 3 deg. Increasing the bin width causes the peak to flatten. The higher contribution around

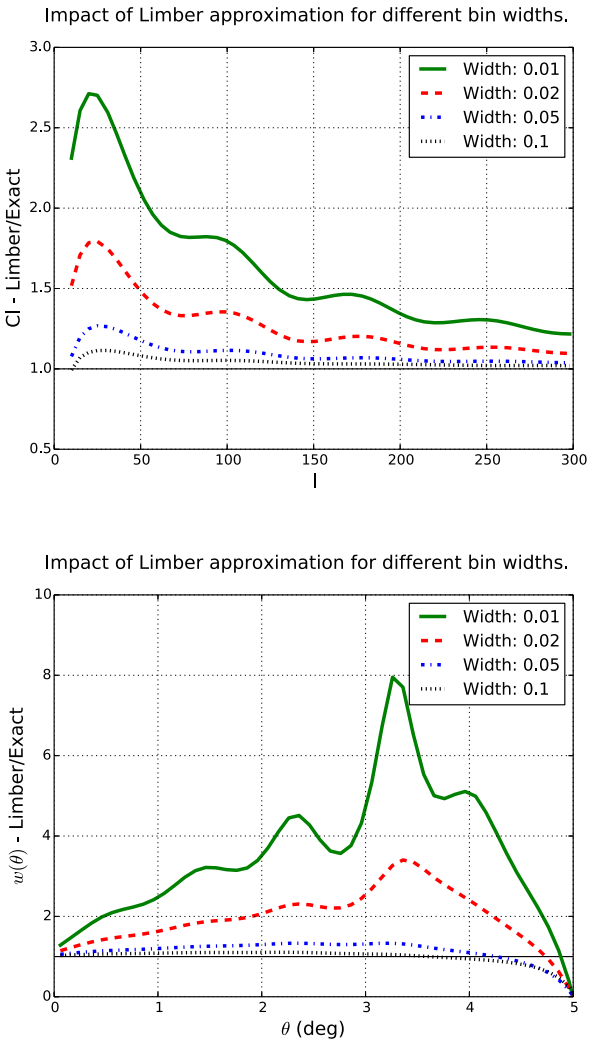

Figure 8. The lines correspond to bin widths 0.01, 0.02, 0.05 and 0.1, centred in $z = 0.5$. Both the exact calculations and the Limber approximation are in real space.

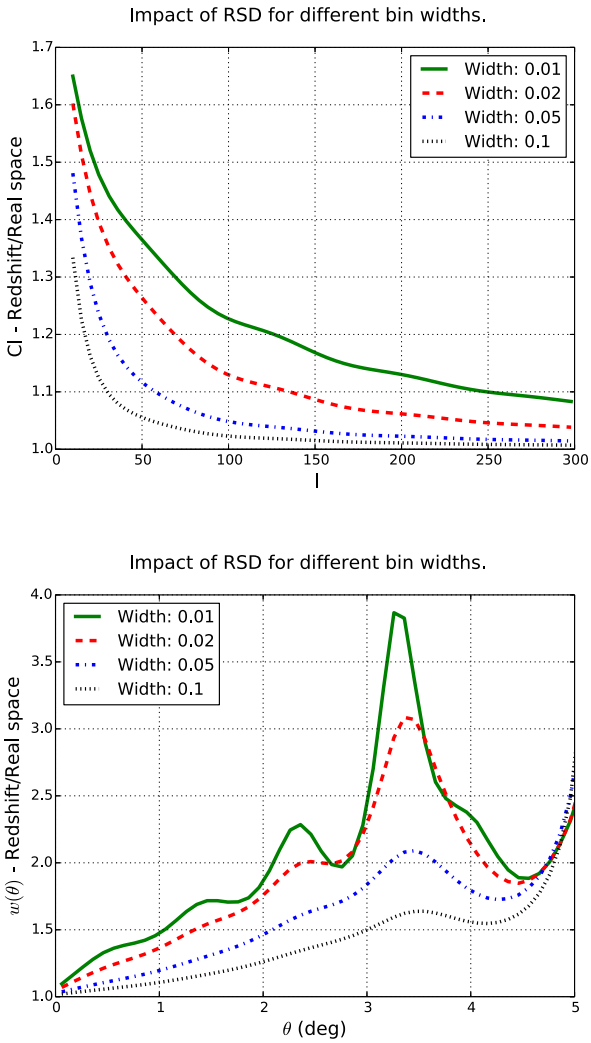

Figure 9. Redshift/real space ratio in Fourier (top) and configuration space (bottom). The lines correspond to redshift bin widths $\Delta z = 0.01, 0.01, 0.02, 0.05, 0.1$, centred around $z = 0.5$. In this figure, ratios about unity mean RSD increases the amplitude.

3.5 deg is caused by BAO in redshift space. From equation (6), the RSD contribution in Fourier space consists of three contributions proportional to spherical Bessel functions of different orders. A small l-value shift gives an angular shift in $w(\theta)$. This results in a BAO contribution in $w(\theta)$ which is shifted in angle. We label this contribution the ghost BAO peak and study its cosmology dependence in Section 4.1.5.

4.1.4 Baryon acoustic oscillations (BAO)

The three panels in Fig. 10 are included to study the impact of BAO. The first panel shows the correlations in Fourier space. One can see how including BAO or using a no-wiggle models leads to oscillation in the ratios. The middle panel shows how the $w(\theta)$ correlation peaks around 4.5 deg for $z = 0.5$, shifting towards lower angles for higher redshifts. One can see that the effect of BAO in redshift space increases when using wider redshift bin. This is counterintuitive, since integrating over the redshift bin results in a convolution in angle. This effect can be understood from RSD. The bottom panel displays the same ratios in real space, where thicker redshift bins lead to a slight decrease in the BAO signal and a shift in the angle due to projection scales. Including RSD increases the correlation amplitude, but lowers the BAO ratio. The last effect occurs since the RSD effect is stronger at lower angles than where BAO peak. For thin bins contribution of RSD has a narrower peak, which explains why thick bins see a higher contribution on BAO in redshift space.

4.1.5 The ghost BAO peak

Fig. 11 illustrates the cosmological dependence of the ghost BAO peak. As shown in Fig. 9, the RSD contribution peaks at different angular values when measured in narrow redshift bins. In the previous figures, we assumed the growth rate $\gamma = 0.55$ of general relativity (GR). Modified gravity models can change the growth rate (Bueno Belloso, García-Bellido & Sapone 2011). Increasing γ leads to a higher amplitude of the clustering, while lowering the effect of RSD. This follows from $\frac{\partial D}{\partial f} < 0$ and $f \equiv \Omega_{\rm m}(z)^{\gamma}$. In Fig. 11, for higher γ the correlations increase for all angles, except around 3.5 deg where the RSD contribution peaks. While being interesting, note that the amplitude difference is low and the effect might be difficult to measure.

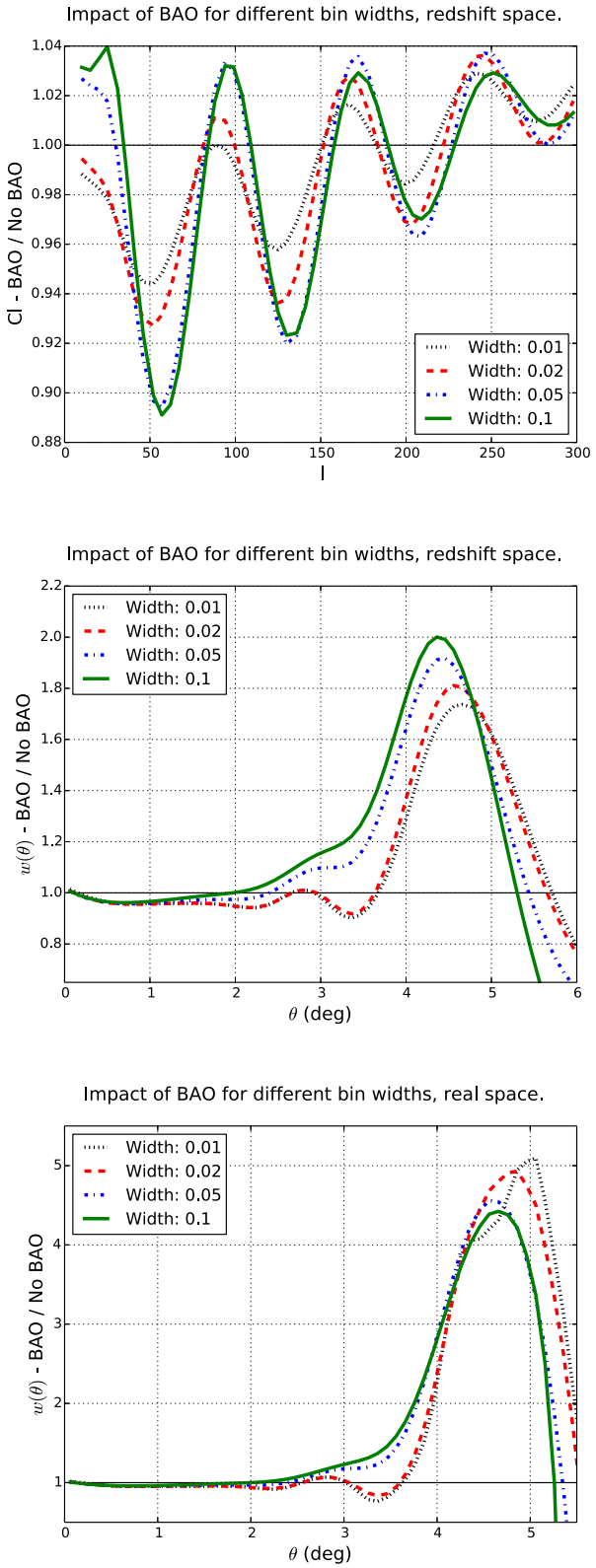

Figure 10. The ratio of correlations including BAO wiggles to a model removing the BAO peak in the EH power spectrum. The first two panels show the ratios in redshift space for C_l and $w(\theta)$. To discuss the effect of RSD on the BAO peak, the third panel shows the angular correlation in real space. All correlations use a mean redshift of $z = 0.5$ and the bin widths $\Delta z = 0.01, 0.02, 0.05, 0.1$.

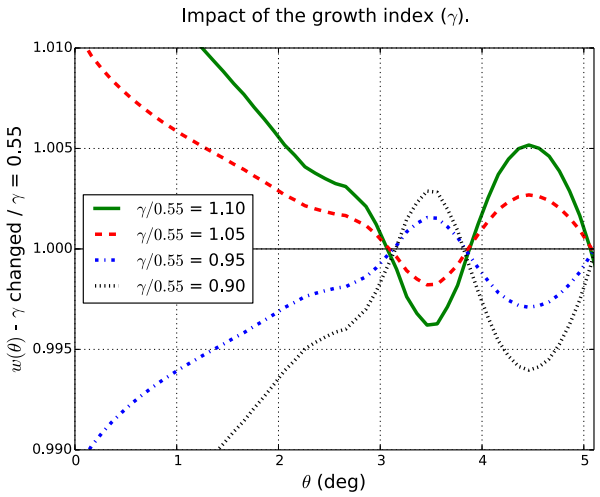

Figure 11. The $w(\theta)$ auto-correlation ratio between a changed growth rate parameter and GR cosmology ($\gamma = 0.55$). The auto-correlation uses a thin bin ($\Delta z = 0.01$), centred in $z = 0.5$. Values of γ in the ratios are ± 5 and ± 10 per cent of the fiducial value (see the legend).

4.2 Cross-correlations between redshift bins

The auto-correlations are the correlation of an observable with itself. Examples are the shear–shear or counts–counts correlation of overdensities in the same redshift bin. A cross-correlation can either come from correlating different quantities as galaxy populations or using different redshift bins for the same quantity. Correlating foreground galaxies with the background shear (Hu & Jain 2004) or correlating two populations of galaxies (McDonald & Seljak 2009; Asorey, Crocce & Gaztañaga 2014) is an example of cross-correlations. In the previous subsection, we studied the auto-correlation of galaxy counts in narrow redshift bins. This subsection focuses on the 2D cross-correlations between galaxy counts in nearby redshift bins.

4.2.1 Amplitude of correlations and comparing effects

The intrinsic correlations between two redshift bins are weaker than the auto-correlations and depend strongly on the separation between the redshift bins. Note that the redshift bin cross-correlations presented here are due to correlations of the matter distribution and not from bins overlapping in photo-z space. This distinction is important if studying photo-z surveys in wide redshift bins. The observed cross-correlations $\tilde{C}_{ij}$ including photo-z effects are approximately (Gaztañaga et al. 2012)

$$\tilde{C}_{ij} \simeq r_{ij} C_{jj} + r_{ji} C_{ii} + r_{ii} r_{jj} C_{ij}, \tag{62}$$

where r_{ij} is the fraction of galaxies actually in bin j, but observed in bin i due to photo-z inaccuracies. If the two first terms dominate, then the cross-correlations are dominated by the tail of the redshift distribution and not the intrinsic cross-correlation.

Fig. 12 shows the cross-correlations where the first bin starts at $z = 0.5$ and the adjacent of two bins. When increasing the bin width from 0.005 to 0.02, which is a factor of 4, the amplitude changes with an order of magnitude in Fourier space. The rapid decline with increasing bin widths is also seen in the angular correlations. In addition, one can see a trend where the small scales are affected more than the BAO scale. The amplitude doubles at 2 deg using a width of 0.005 instead of 0.01, while the change is 30 per cent at the BAO peak.

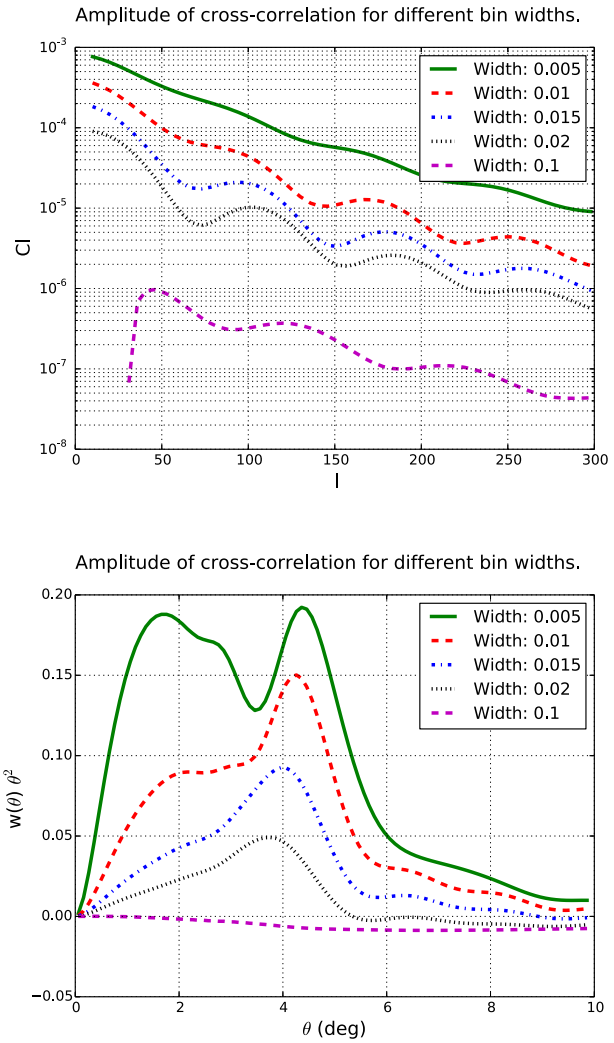

Figure 12. Amplitude of cross-correlations between adjacent redshift bins with equal redshift width. The first redshift bin starts at $z = 0.5$ and the five lines correspond to bin widths $\Delta z/(1+z) = 0.005, 0.01, 0.015, 0.02, 0.1$. The top and bottom panels, respectively, respectively show the C_l and $w(\theta)$ correlations. Here $\Delta z = 0.01$ corresponds to the default forecast binning of a spectroscopic sample, while $\Delta z/(1+z) = 0.005$ is included to motivate the potential gain by using even thinner redshift bins.

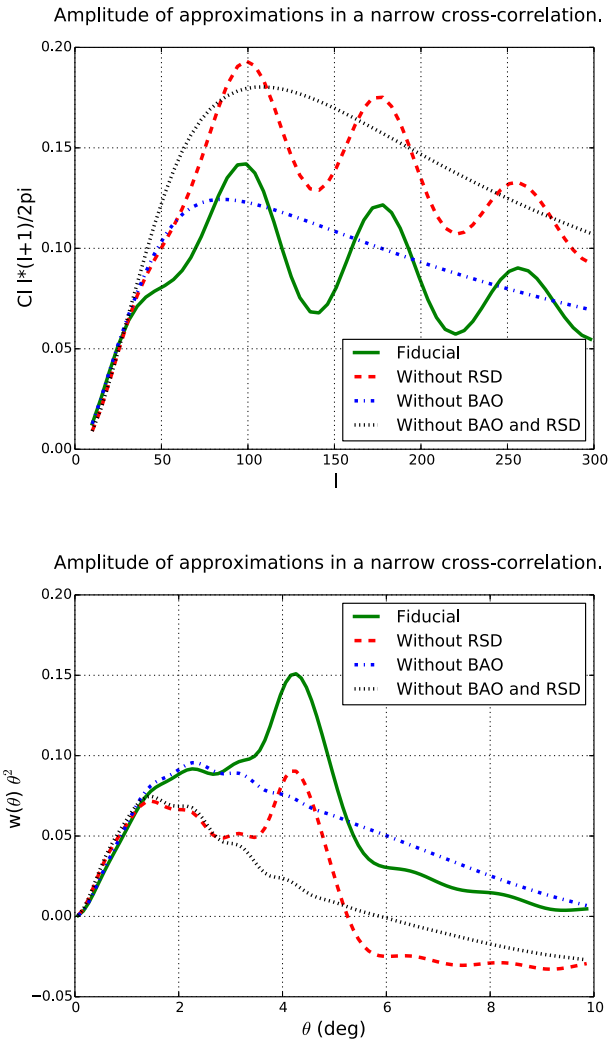

Figure 13. Cross-correlations between adjacent redshift bins. Both bins are $\Delta z = 0.01(1+z)$ wide and the first bin starts at $z = 0.5$. The four lines include different effects, with the fiducial line including both RSD and BAO. The top and bottom panels, respectively, show C_l and $w(\theta)$.

Fig. 13 demonstrates how the cross-correlations are affected by BAO, RSD and both effect together. These effects are also strong in the cross-correlations. In the auto-correlations, the effect of RSD increased when decreasing the redshift bin width. Fig. 14 shows the effect of RSD for three different bin widths. The effect of RSD depends strongly on the separation. Also, for thinner bins the RSD suppresses the signal down to smaller angles. In $w(\theta)$ the negative correlation comes from the squashing in the radial direction that creates a deficit of galaxy pairs and a region of negative correlations (see fig. 2 in Gaztañaga et al. 2012).

4.2.2 Baryon acoustic oscillations

A characteristic effect in the cross-correlations is an enhancement of BAO. While the effect is present in Fourier space, the physical explanation is simpler in configuration space. Fig. 15 shows together an auto- and cross-correlation with and without BAO. Around 1 deg the auto- and cross-correlations differ by a factor of 2, while they

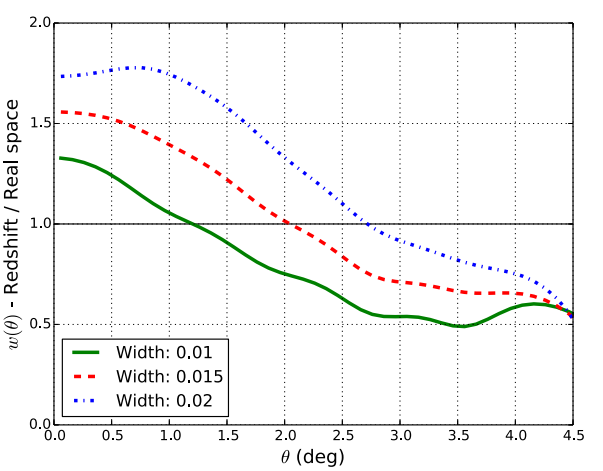

Figure 14. Redshift/real space ratios for the cross-correlation of galaxy counts between adjacent bins. The first bin starts at $z = 0.5$ and the three lines correspond to $\Delta z/(1+z) = 0.01, 0.015, 0.02$. Ratios below unity mean the RSD suppress the cross-correlations.

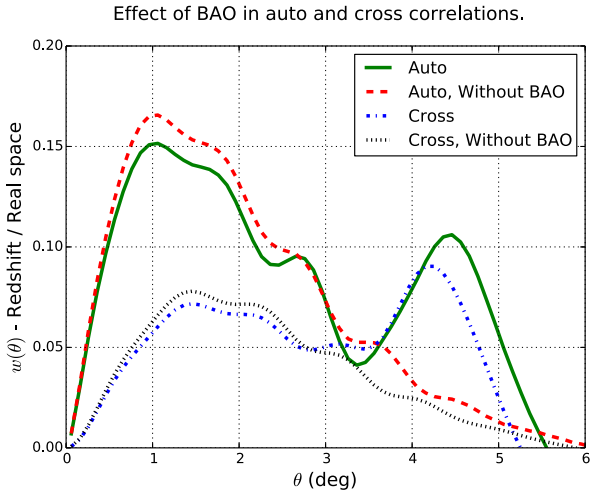

Figure 15. Effect of BAO in the auto- and cross-correlations. The auto-correlations start at $z = 0.5$ with $\Delta z = 0.01(1 + z)$. In the cross-correlation, the second bin is the adjacent bins, which also use $\Delta z = 0.01(1 + z)$. Both the auto- and cross-correlations are shown with and without BAO.

are comparable around the BAO peak. A geometrical interpretation follows from the galaxy pair separation. The galaxy pair separation r can be decomposed into

$$r^2 = r_\parallel^2 + r_\perp^2, \tag{63}$$

where $r_\parallel$ and $r_\perp$ are the distance parallel and perpendicular to the line of sight. The $r_\perp$ is measured in an angular separation θ (on the sky) and converted to a distance through $r_\perp \approx \chi(z)\theta$, with $\chi(z)$ being the comoving distance to the closest galaxy. Looking at one fixed angle for the BAO scale corresponds roughly to selecting galaxy pairs with one transverse separation. Galaxy pairs within a thin redshift bin are mostly radially separated around the BAO scale, therefore measuring the angular diameter distances. The cross-correlations between close redshift bins are dominated by the radial BAO, therefore measuring the comoving distance (Gaztañaga, Cabré & Hui 2009).

The auto- and cross-correlations differ radically in the $r_\parallel$ distribution of galaxy pairs. For the auto-correlation in ΔR wide top-hat bins, the probability is highest for zero radial separation and decreases linearly towards zero at the bin edges. In the cross-correlation of adjacent bins, the highest probability corresponds to $r_{||} = \Delta R$ and decreases linearly towards the lowest and highest separations. For cross-correlations, the redshift bin separation acts as a filter around a characteristic distance. In Fig. 15, the result can be seen from the small scales being suppressed, while the change is less around the BAO scale.

The cross-correlations also filter away small scales when the bins are separated, although the distribution of radial distances ($r_\parallel$) changes. Fig. 16 includes the cross-correlations between more bins. For larger redshift bin separation, the suppression of small scales in the cross-correlations becomes stronger. On the other hand, for the BAO scale the first cross-correlations are comparable to the auto-correlations. Here the gap between two redshift bins introduces a lower limit on the galaxy pair separation. As the separation between the bins increases, the distance filtered out gradually grows above the BAO scale of 150 Mpc. For larger separation, as seen in the last cross-correlations, the peak is also affected.

For angles above 3.5 deg, the last cross-correlation in Fig. 16 becomes negative. Unlike the auto-correlation which is positive (for the relevant angles), the cross-correlation can also be negative. In

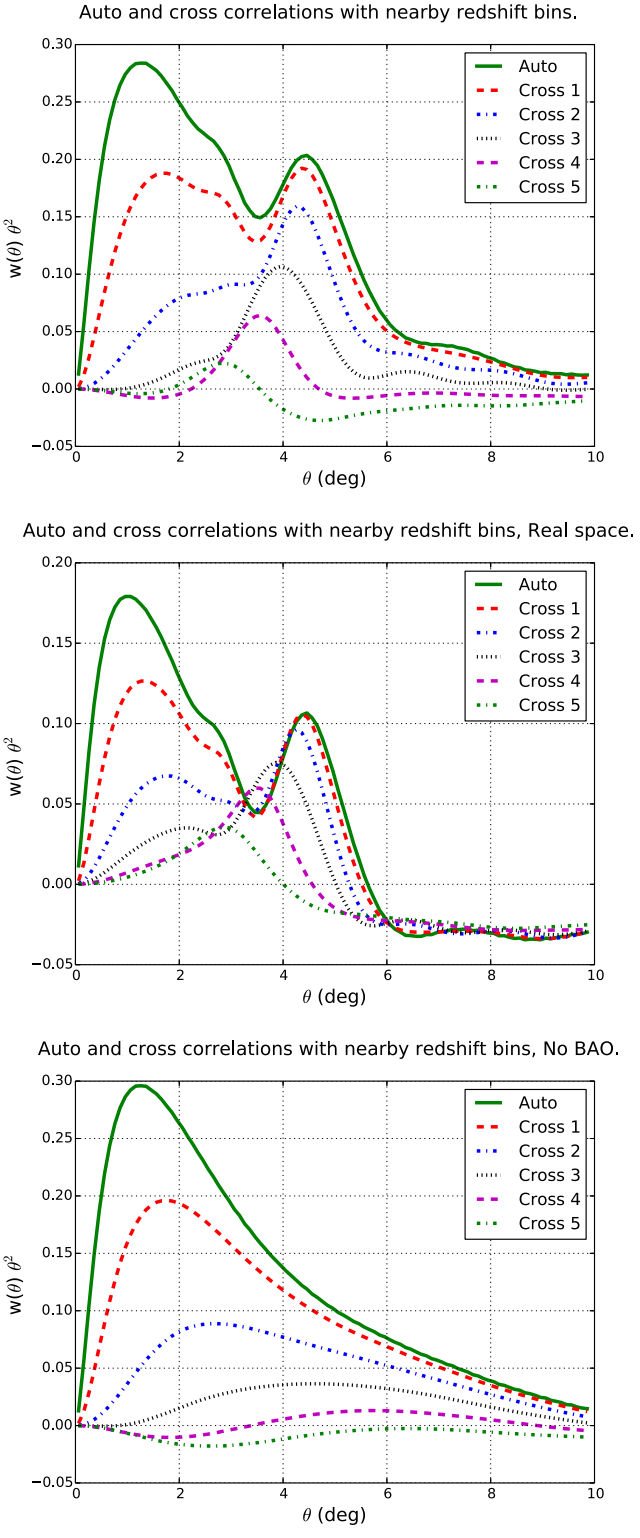

Figure 16. The auto- and cross-correlations between close redshift bins. The first redshift bin always starts at $z = 0.5$ and all the redshift bin widths are $\Delta z = 0.005(1 + z)$. We show the auto-correlation (auto) and correlation with the adjacent bin (cross 1) and the four next closest redshift bins at higher redshift. In the legend, 'cross n' means the redshift bin index of the two observable differs with n, i.e. 1 is the adjacent bin. The top, middle and bottom panels show, respectively, the fiducial, real space and no-wiggle correlations.

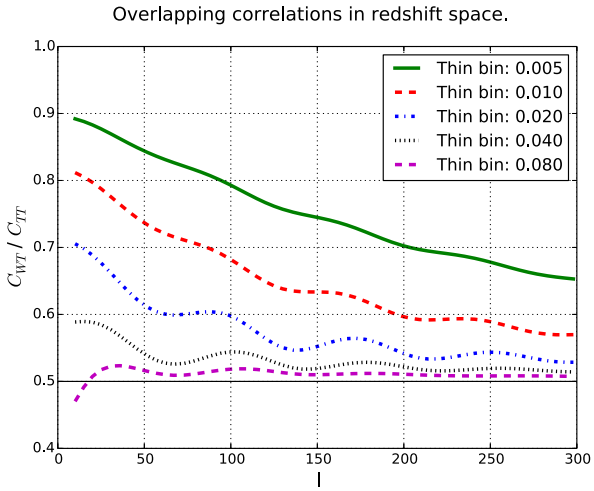

Figure 17. Ratio $C_{\rm WT}/C_{\rm TT}$ where W and T are a wide and thin bin. Both bins are centred around $z = 0.5$, with $\Delta Z_{\rm Thick} = 2\Delta Z_{\rm Thin}$. The lines correspond to using $\Delta z/(1+z) = 0.005, 0.01, 0.02, 0.04, 0.08$ for the thinnest redshift bin.

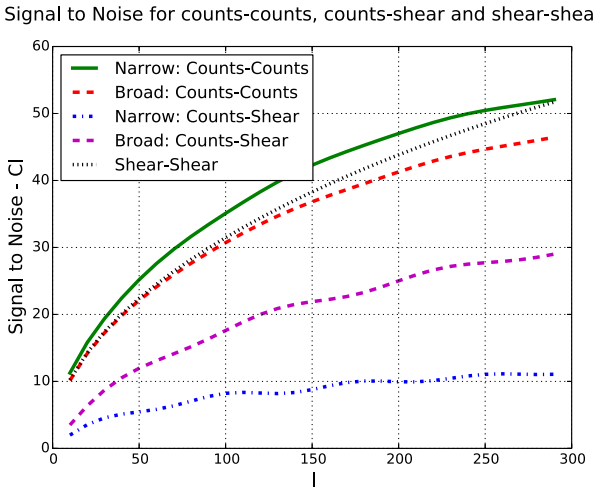

Figure 18. S/N for different types of correlation. Two galaxy populations are included, a foreground population for measuring galaxy counts and a background population for faint galaxies. In two lines corresponding to counts–counts and counts–shear, a thin bin of $\Delta z = 0.001, 0.5$ is used, while the other two use a thick bin of $\Delta z = 0.01, 0.5$. The background bin at $z = 1.1$ is $\Delta z = 0.15$ wide. This figure also shows the shear–shear S/N ratio for the background shear used for both the counts–shear correlations.

Fourier space (C_l), the negative cross-correlations can be understood from the spherical Bessel function in equations (2) and (3). For an infinitesimal thin redshift bin, the fluctuations $\delta_l(z, k)$ are proportional to $j_l(kr(z))$, where $r(z)$ is the comoving distance to the redshift bin. When cross-correlating two redshifts the oscillations might be out of phase, which generates a negative contribution. The integral over the redshift bins is (in real space) a linear superposition of two such Bessel functions. For thick bins negative contributions average out and thin redshift bins increase the probability of finding negative correlations.

4.2.3 Partial overlapping bins

The correlations discussed so far have either been auto-correlations or cross-correlations of non-overlapping redshift bins. One can for galaxy counts use a multi-tracer strategy and split the galaxy sample into different populations. For example, including two galaxy populations with very different biases reduces the sample variance. In the forecast, we use the spectroscopic and photometric surveys as two different populations. The spectroscopic binning is seven times thinner (than the photometric sample) to capture the radial information. When cross-correlating overlapping photometric and spectroscopic surveys, it naturally leads to cross-correlations of redshift bins with different widths.

Fig. 17 shows the cross-correlation of galaxy counts in two overlapping redshift bins with $\Delta Z_{\rm Wide} = 2\Delta Z_{\rm Thin}$. The ratio shown is $C_{\rm WT}/C_{\rm TT}$, where T and W, respectively, denote wide and thin bins. In the Limber approximation, the auto-correlation is inversely proportional to the bin width. If all the correlation of the overlapping cross-correlation is due to galaxy pairs in the overlapping region, one expects $C_{\rm WT}/C_{\rm TT} = 0.5$ for the Limber approximation in real space. For the relatively thick bins of $\Delta z = 0.04, 0.05$, the ratio is close to the Limber ratio (0.5). Cross-correlation of thinner bins increases the ratio. For the three thin redshift bins of 0.005, 0.01 and 0.02, the overlapping correlation is higher than what is expected from counting galaxy pairs in the overlapping region. When using two overlapping bins, the galaxies are correlating inside the overlapping redshift region, therefore increasing the correlation, but there is also a contribution for the regions which doesn't overlap.

4.3 Errors and S/N

The cosmic variance errors when assuming Gaussian fluctuations are (Dodelson 2003)

$$\mathrm{Cov}(C_{ij}, C_{mn}) = N^{-1}(l)\left(C_{im}C_{jn} + C_{in}C_{jm}\right) \tag{64}$$

$$\mathrm{Var}(C_{ij}) = N^{-1}(l)\left(C_{ii}C_{jj} + C_{ij}^2\right) \tag{65}$$

$$\mathrm{Var}(C_{ii}) = 2N^{-1}(l)C_{ii}^2, \tag{66}$$

where $N(l) = 2f_{\rm sky}(2l+1)$ is the number of modes and $f_{\rm sky}$ is the sky fraction covered by the survey. The first line gives the general covariance expression, while the second and third lines, respectively, give the variance for an auto- and cross-correlation. Additionally, the counts–counts correlation ($C_{g_i g_j}$) includes a shot noise from sampling a finite number of galaxies and shape measurement errors affect the shear–shear correlations. Let $\tilde{C}$ and C, respectively, denote the correlations including or not the measurement errors. The observed correlations are

$$\tilde{C}_{g_i g_j} = C_{g_i g_j} + \delta_{ij}\frac{1}{N_i} \tag{67}$$

$$\tilde{C}_{\gamma_i \gamma_j} = C_{\gamma_i \gamma_j} + \delta_{ij}\frac{\sigma_\gamma^2}{N_i}, \tag{68}$$

where N_i is the observed galaxy number in bin i per steradian and σ_γ^2 is the average shear measurement variance.

Fiducially to match the forecast, we assume a 0.4 galaxies per arcmin^2 dense sample magnitude limited to $i_{\rm AB} < 22.5$ and a galaxy bias of $b(z) = 2 + 2(z - 0.5)$. The correlation in this subsection uses $z = 0.5$, which means $b = 2$. These values are selected to match the spectroscopic sample in the forecast. Note that the errors shown in Fig. 18 are dominated by cosmic variance. The exact $n(z)$ details (see Paper II) are therefore less important. All S/N plots assume 1000 sq. deg. survey area.

Fig. 18 shows the S/N for different counts–counts, counts–shear and shear–shear correlations. An important point of this figure is to compare how the redshift bin width affects the S/N . Therefore, the

counts–counts and counts–shear correlations are both shown with a thin and a thick foreground bin (see the caption). For zero shot noise, the S/N of the counts–counts auto-correlations are

$$(\mathrm{S/N})[C_{g_i g_i}] \equiv \sqrt{N(l)/2} \tag{69}$$

which is independent of the redshift bin width. The two counts–counts auto-correlation lines differ in shot noise covering different redshifts since one set of bins are wider. Except this, the S/N for the two auto-correlations does not depend on the redshift bin width. The counts–shear S/N is directly dependent on the lens bin width. From the Limber approximation, the counts–counts auto-correlation in the variance is inversely proportional to the bin width ($C_{ii} \propto 1/\Delta_i$). On the other hand, the counts–shear signal is independent of the foreground bin width when ignoring the cosmological evolution in the lens bin. Combining these two expressions leads to

$$(\mathrm{S/N})[C_{g_i \gamma}] \propto \sqrt{\Delta_i}, \tag{70}$$

where Δ_i is the redshift bin width. This means the S/N of a single counts–shear cross-correlation decreases when using a thinner lens redshift bin. In Fig. 18, the two counts–shear S/N lines use $\Delta z = 0.01$ and 0.1 wide lens bins. A cross-correlation with 10 times thinner redshift bins should result in around three times lower S/N. While each correlation becomes noisier when decreasing the lens bin width, the reduced width allows for more bins. The number of bins is proportional to $1/\Delta_i$. Therefore, the combined S/N for all counts–shear correlations scales with $\sqrt{\Delta_i}$. In addition, thinner lens bins have the advantage of less projection in redshift.

Section 4.2 described the galaxy counts cross-correlation between adjacent redshift bins. These correlations can, if the S/N is sufficient, measure radial information. The S/N for the cross-correlations between different redshift bins are directly related to the cross/auto-correlation ratio. This follows from

$$\frac{(\mathrm{S/N})[C_{ij}]}{(\mathrm{S/N})[C_{ii}]} = \sqrt{2}\frac{C_{ij}}{C_{ii}}\frac{C_{ii}}{\sqrt{C_{ii}C_{jj} + C_{ij}^2}} \tag{71}$$

$$\approx \sqrt{2}\frac{C_{ij}}{C_{ii}}\left(1 + \left(\frac{C_{ij}}{C_{ii}}\right)^2\right)^{-1/2} \tag{72}$$

$$\approx \sqrt{2}\frac{C_{ij}}{C_{ii}}, \tag{73}$$

where the second and third lines, respectively, use $C_{ii} \approx C_{jj}$ and $C_{ij} \ll C_{ii}$. Approximating the auto-correlations ($C_{ii} \approx C_{jj}$) works for equally wide and thin bins. When $C_{ii}/C_{ij} = 2.1$, 6.9 the last approximation is respectively accurate to 10 and 1 per cent. The S/N ratio can be understood from the cross-correlation variance being dominated by the auto-correlation variance.

Fig. 19 (top panel) shows the ratio C_{ij}/C_{ii} for various bin widths. When increasing the bin width, the ratio declines quickly due to C_{ij} being sensitive to the redshift bin separation. If using $\Delta z = 0.005$ instead of $\Delta z = 0.01$, the C_{ij}/C_{ii} ratio doubles. The bottom panel shows the $w_{ij}(\theta)/w_{ii}(\theta)$ ratios. Another interesting aspect is the large $w(\theta)$ cross-correlation signal at large angles. For example, the cross-correlation with bin width of 0.01 is 40 per cent of the auto-correlation at 2 deg and 80 per cent at 4 deg. This means the cross-correlation is gaining a higher S/N at larger angles.

To illustrate the effect of cross-correlations, Fig. 20 shows the S/N for extremely thin redshift bins. These redshift bins are $\Delta z = 0.001(1+z)$ wide, which would correspond to 694 redshift bins for $0.1 < z < 1.2$. From the figure, one can see that there is a sharp drop in S/N when increasing the distance between the redshift bins. Also, the change is lower at low l-values, which make the

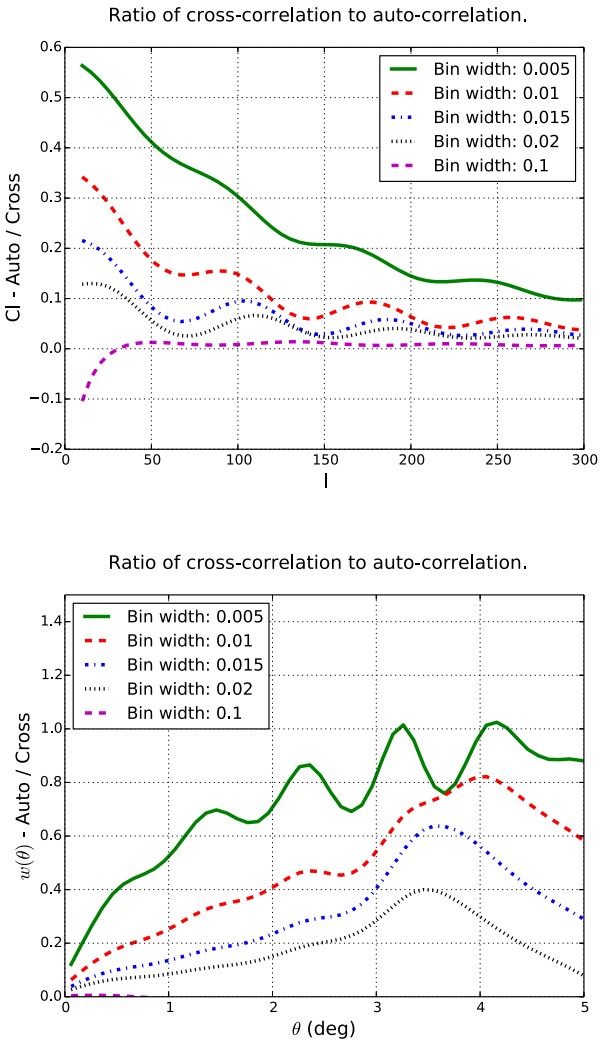

Figure 19. Auto/cross-correlation ratio for galaxy counts. The auto-correlation bin starts at $z = 0.5$, with the four lines corresponding to $\Delta z = 0.005$, 0.01, 0.015, 0.02. The cross-correlation is between the auto-correlation bin and the adjacent bin at higher redshift. Both redshift bins are equally wide. The top and bottom panels, respectively, show the ratio in Fourier and configuration space.

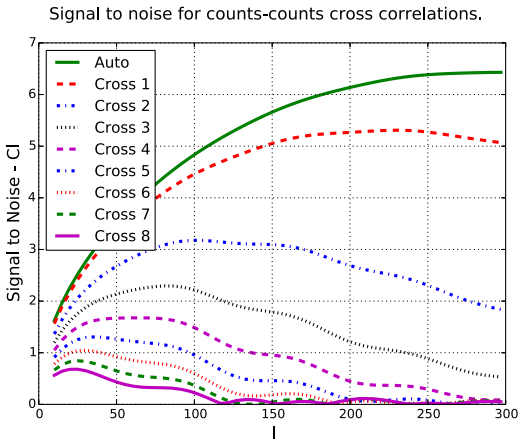

Figure 20. Cross-correlations between very narrow redshift bins. All bins are $\Delta z = 0.001(1+z)$ wide and the first redshift bin starts at $z = 0.5$. The auto-correlation is for the first redshift bin, while 'cross X' corresponds to a cross-correlation of the first bin with a bin separated by X times Δz.

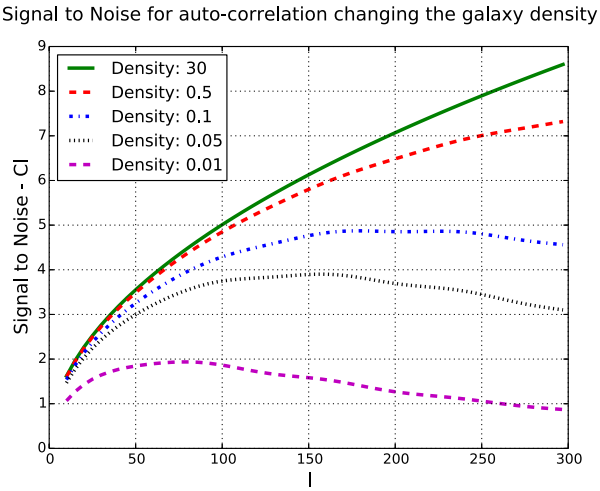

Figure 21. S/N for different galaxy densities. The auto-correlation redshift bin is centred in $z = 0.5$ and is $\Delta z = 0.01(1 + z)$ wide. The S/N is calculated for 0.01, 0.05, 0.1, 0.5 and 30 galaxies per arcmin^2 in the full sample. In addition, 50 per cent is removed to simulate various cuts.

cross-correlations more important at large scales. For the forecast in $\Delta z = 0.01(1 + z)$ wide bins, the main contribution comes from the auto-correlation and cross-correlation with the adjacent bin.

Finally Fig. 21 shows the S/N for auto-correlations in the redshift bin $z = 0.5$, $\Delta z = 0.01(1 + z)$ for different densities. The upper line with 30 galaxies per arcmin^2, which is lower than the expected LSST density of 40 galaxies arcmin^2 (LSST Science Collaboration 2009), is approximately noiseless for the counts–counts auto-correlation. A line with 0.5 galaxies per arcmin^2 is close to the spectroscopic density used in the forecast (0.4 galaxies per arcmin^2). For the l-values considered for the forecast ($l \leq 300$), the dense spectroscopic sample has an S/N close to the noiseless limit. This conclusion does however vary with $l_{\rm max}$ and also with the redshift.

5 CONCLUSION

In this paper, we have studied the modelling of galaxy clustering, RSD and WL with angular cross-correlations. Lensing is often studied using 2D correlations, while clustering and RSD are analysed with the 3D power spectrum. Combining WL, large-scale structure and RSD is from a theoretical viewpoint significantly easier using the angular correlation functions. Directly constructing observable in angles (or multipoles) and redshifts avoids the model assumptions that are needed in a 3D analysis when converting distances. Moreover, the expression for the covariance is straightforward. Using only angular correlations avoids double counting transverse information and can naturally account for potential redshift uncertainties in the large-scale structure analysis by migration matrices (Gaztañaga et al. 2012).

One practical concern is the efficiency of implementing a computer code for predicting the angular correlation function. Analysing a spectroscopic sample using 2D correlations requires a large number of redshift bins to capture the radial information. In Section 3 we introduced an algorithm specialized in calculating the cross-correlations between many redshift bins and with multiple tracers. Instead of calculating each correlation separately, all correlations are calculated at once. This allows for reusing parts of the calculations and extensive use of matrix multiplication. In particular, the integration between all correlation of redshift bins is expressed using a matrix product. Being formulated in terms of array operations and matrix multiplications allows for an efficient implementation, even in high-level languages (e.g. PYTHON) with bindings to high-performance linear algebra implementations.

Section 4 began with studying the effect of BAO, RSD and the Limber approximation for the auto- and cross-correlations. For the auto-correlation of $\Delta z = 0.1$ thick bins, the Limber approximation can be sufficient for a small-area survey. In narrow redshift bins ($\Delta z = 0.01$), which is needed for the forecast, the Limber approximation completely breaks down. RSD leads to 30 per cent larger amplitude for the galaxy counts auto-correlations in broad bins. For thin bins ($\Delta z = 0.01$), the RSD effect can result in 2.5–3 times higher auto-correlations at low multipoles. In addition, for thinner bins the effect of RSD clearly shows a peak in angle. We showed that this second peak, which we named the ghost BAO peak, results from the BAO peak being shifted in redshift space.

The cross-correlation of nearby redshift bins unexpectedly has a larger BAO contribution than the auto-correlations. When cross-correlating two redshift bins, the bin separation affects the radial pair separation. In cross-correlations, the most probable radial galaxy separation is the distance between the mean of the two redshift bins. Therefore, cross-correlations include pairs with higher radial separation, which suppress small-scale clustering and lead to a larger BAO contribution. Galaxy pairs within a thin redshift bin are mostly radially separated around the BAO scale, therefore measuring the angular diameter distances. The cross-correlations between close redshift bins are dominated by the radial BAO, which measures the comoving distance (Gaztañaga et al. 2009). We have also shown in Section 4.3 that the S/N is larger in the cross-correlation at BAO scales.

We also studied the S/N for different correlations. The counts–counts correlations have the highest S/N, while the counts–shear and shear–shear correlations have a lower S/N ratio. In the count–shear correlation the bin width of the galaxy counts in the lens bin directly affects the noise, while the signal is only affected by projection effects. Each correlation of narrow bins has a lower S/N. However, the total S/N is higher since the thinner bins result in more counts–shear cross-correlations. Finally, we looked at the sensitivity of galaxy density for the counts–counts auto-correlations. For a dense galaxy sample (0.4 galaxies per arcmin^2), used for the spectroscopic sample in the forecast, the S/N for $z = 0.5$ is close to the noiseless limit.

Altogether our results show that this new approach to clustering analysis, using angular cross-correlations in narrow redshift bins, is potentially viable: it recovers all the 3D information (Asorey et al. 2012, 2014), it can be predicted with fast algorithms and it contains new insights of physical effects such as WL, RSD and BAO. In the following papers of this series, we will present different applications and results using the formalism presented here.

ACKNOWLEDGEMENTS

We would like to thank Martin Crocce for help with the initial stages of this long project. Funding for this project was partially provided by the Spanish Ministerio de Ciencia e Innovacion (MICINN), project AYA2009-13936 and AYA2012-39559, Consolider-Ingenio CSD2007-00060, European Commission Marie Curie Initial Training Network CosmoComp (PITN-GA-2009-238356) and research project 2009-SGR-1398 from Generalitat de Catalunya. ME acknowledges support from the European Research Council under FP7 grant number 279396. He was also supported by an FI grant from Generalitat de Catalunya.

REFERENCES

Abdalla F. et al., 2012, preprint (arXiv:1209.2451)
Amendola L. et al., 2013, Living Rev. Relativ., 16, 6
Amiaux J. et al., 2012, Proc. SPIE, 8442, 84420Z
Anderson L. et al., 2014, MNRAS, 439, 83
Asorey J., Crocce M., Gaztañaga E., Lewis A., 2012, MNRAS, 427, 1891
Asorey J., Crocce M., Gaztañaga E., 2014, MNRAS, 445, 2825
Bartelmann M., Schneider P., 2001, Phys. Rep., 340, 291
Bernstein G. M., Cai Y.-C., 2011, MNRAS, 416, 3009
Blas D., Lesgourgues J., Tram T., 2011a, Astrophysics Source Code Library, record ascl:1106.020
Blas D., Lesgourgues J., Tram T., 2011b, J. Cosmol. Astropart. Phys., 7, 34
Bueno Belloso A., García-Bellido J., Sapone D., 2011, J. Cosmol. Astropart. Phys., 10, 10
Cai Y.-C., Bernstein G., 2012, MNRAS, 422, 1045
Challinor A., Lewis A., 2011a, Astrophysics Source Code Library, record ascl:1105.013
Challinor A., Lewis A., 2011b, Phys. Rev. D, 84, 043516
Crocce M., Fosalba P., Castander F. J., Gaztañaga E., 2010, MNRAS, 403, 1353
Crocce M., Cabré A., Gaztañaga E., 2011, MNRAS, 414, 329
Crocce M., Scoccimarro R., Bernardeau F., 2012, MNRAS, 427, 2537
de Putter R., Doré O., Takada M., 2013, preprint (arXiv:1308.6070)
Di Dio E., Montanari F., Lesgourgues J., Durrer R., 2013, J. Cosmol. Astropart. Phys., 11, 44
Dodelson S., 2003, Modern Cosmology. Academic Press, New York
Eisenstein D. J., Hu W., 1998, ApJ, 496, 605
Eriksen M., Gaztañaga E., 2015, MNRAS, 452, 2168, (Paper II)
Fisher K. B., Scharf C. A., Lahav O., 1994, MNRAS, 266, 219
Fisher K. B., Huchra J. P., Strauss M. A., Davis M., Yahil A., Schlegel D., 1995, ApJS, 100, 69
Font-Ribera A., McDonald P., Mostek N., Reid B. A., Seo H.-J., Slosar A., 2013, preprint (arXiv:1308.4164)
Fosalba P., Gaztañaga E., Castander F. J., Manera M., 2008, MNRAS, 391, 435
Fu L. et al., 2008, A&A, 479, 9
Gaztañaga E., Cabré A., Hui L., 2009, MNRAS, 399, 1663
Gaztañaga E., Eriksen M., Crocce M., Castander F. J., Fosalba P., Marti P., Miquel R., Cabré A., 2012, MNRAS, 422, 2904
Hamilton A. J. S., 1998, in Hamilton D., ed., Astrophysics and Space Science Library, Vol. 231, The Evolving Universe. Kluwer, Dordrecht, p. 185
Heymans C. et al., 2013, MNRAS, 432, 2433
Hu W., Jain B., 2004, Phys. Rev. D, 70, 043009
Ivezic Z. et al., 2008, preprint (arXiv:0805.2366)
Jeong D., Komatsu E., Jain B., 2009, Phys. Rev. D, 80, 123527
Kaiser N., 1987, MNRAS, 227, 1
Kilbinger M. et al., 2013, MNRAS, 430, 2200
Kirk D., Lahav O., Bridle S., Jouvel S., Abdalla F. B., Frieman J. A., 2013, preprint (arXiv:1307.8062)
Laureijs R. et al., 2011, preprint (arXiv:1110.3193)
Le Fèvre O. et al., 2013, A&A, 559, A14
Lesgourgues J., 2011a, preprint (arXiv:1104.2932)
Lesgourgues J., 2011b, preprint (arXiv:1104.2934)
Lesgourgues J., Tram T., 2011, J. Cosmol. Astropart. Phys., 9, 32
Levi M. et al., 2013, preprint (arXiv:1308.0847)
Lewis A., Challinor A., Lasenby A., 2000, ApJ, 538, 473
Limber D. N., 1954, ApJ, 119, 655
Loverde M., Afshordi N., 2008, Phys. Rev. D, 78, 123506
LSST Science Collaboration, 2009, preprint (arXiv:0912.0201)
McDonald P., Seljak U., 2009, J. Cosmol. Astropart. Phys., 10, 7
Martí P., Miquel R., Castander F. J., Gaztañaga E., Eriksen M., Sánchez C., 2014, MNRAS, 442, 92
Padmanabhan N. et al., 2007, MNRAS, 378, 852
Parkinson D. et al., 2012, Phys. Rev. D, 86, 103518
Schlegel D. J. et al., 2009, preprint (arXiv:0904.0468)
Schlegel D. et al., 2011, preprint (arXiv:1106.1706)
Smith R. E. et al., 2003, MNRAS, 341, 1311
Takahashi R., Sato M., Nishimichi T., Taruya A., Oguri M., 2012, ApJ, 761, 152
Taylor A. N., Heavens A. F., 1995, in Holt S. S., Bennett C. L., eds, AIP Conf. Ser. Vol. 336, Dark Matter. Am. Inst. Phys., New York, p. 381
Tram T., Lesgourgues J., 2013, J. Cosmol. Astropart. Phys., 10, 2

APPENDIX A: AUTO- AND CROSS-CORRELATIONS

A1 Redshift space distortions

The RSD dependence on the redshift bin width is illustrated in Fig. A1. An additional redshift from peculiar line-of-sight velocities can move galaxies between redshift bins, which cause the RSD signal. In thin redshift bins, more galaxies move between the bins; therefore, thin bins increase the RSD signal. For the thinnest bin ($\Delta z = 0.005$), the auto-correlation has double the amplitude in redshift compared to real space. When increasing the bin width, both the signal and fraction of RSD signal decrease. For cross-correlations, the RSD can contribute positively or negatively, depending on the bin width. In this configuration, below $\Delta z \approx 0.015$, the RSD increases the cross-correlation, suppressing the signal for wider redshift bins. For thick redshift bins ($\Delta z = 0.05$–0.1), the cross-correlation is negative in redshift space.

Fig. A2 shows a $w(\theta)$ cross-correlation amplitude when shifting one redshift bin, while the other is centred around $z = 0.5$. In the top panel, both redshift bins are $\Delta z = 0.01$ wide and the inner vertical lines mark the fixed bin. For two narrow and fully overlapping bins, the signal doubles in redshift space. When reducing the amount of overlap, both the clustering in real space and redshift space decreases. The two outer vertical lines mark having redshift bins side by side. In this configuration, the correlations are still positive. For larger separation, the RSD suppress the signal, which was also seen in Fig. A1.

In the bottom panel, the fixed bin is thick ($\Delta z = 0.1$), while the bin changing position is still thin ($\Delta z = 0.01$). For fully overlapping bins and close centres, the signal is fairly flat. When the thin bins move closer to the edge, but they still overlap, the signal falls off sharply. The decrease in the cross-correlation amplitude comes from removing part of the non-overlapping cross-correlations between the bins. When the bins move apart, the signal clearly becomes negative in redshift space.

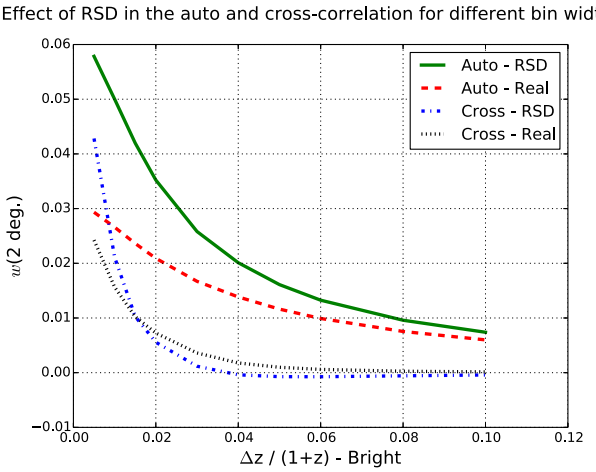

Figure A1. Contribution of RSD for the auto- and cross-correlations with the adjacent bin when varying the redshift bin width. Both redshift bins are equally wide (at $z = 0$), with the width given on the x-axis. The correlations are shown at 2 deg and the first redshift bin starts at $z = 0.5$.

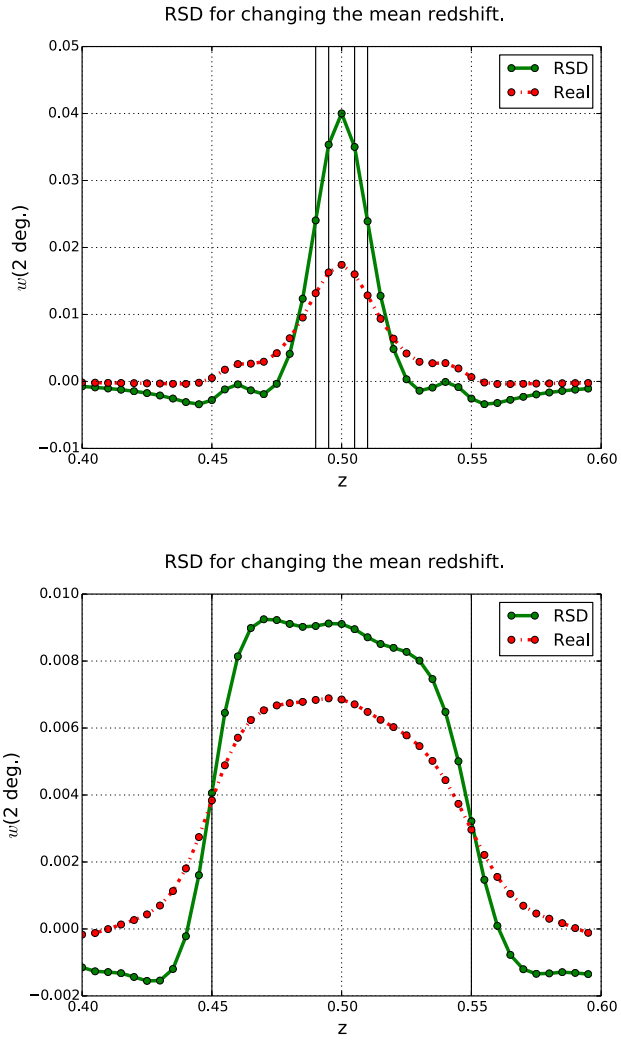

Figure A2. The cross-correlation when changing one bin position. In both panels, one redshift bin is fixed at $z = 0.5$ and the second varies as indicated on the x-axis. The top panel correlates two thin ($\Delta z = 0.01$) redshift bins. The two inner vertical lines ($z = 0.495, 0.505$) mark the fixed redshift bin, while the two outer lines ($z = 0.49, 0.51$) mark when the bins have no redshift overlap. In the bottom panel, the fixed bin is thick ($\Delta z = 0.1$), while the varying bin is thin ($\Delta z = 0.01$). In the fixed bin, the bias $b(z) = 1.2 + 0.4(z - 0.5)$ is used. Here the vertical lines ($z = 0.45, 0.55$) mark the fixed bin. The two lines show the correlation in redshift and real space.

A2 Non-linear effects

Non-linear gravitational effects enhance the dark matter power spectrum on small scales. The EH and CAMB (Lewis, Challinor & Lasenby 2000) power spectrum models only the linear power spectrum. For modelling the non-linear effects, one can create fitting formulas based on N-body simulations or use perturbation theory. The Halofit-II power spectrum model is based on a series of simulations to model non-linear gravitational effects (Smith et al. 2003; Takahashi et al. 2012). To include the Halofit only requires implementing the model and providing a linear power spectrum, for which we use the EH.

Fig. A3 shows the non-linear/linear C_l ratios. The ratios are for auto- and adjacent cross-correlations in the redshift bins $z = 0.5$, 0.6, 1.0 and with $\Delta z = 0.01$. The non-linear effects in the power spectrum increase with the comoving wavenumber ($k \equiv l/\chi(z)$).

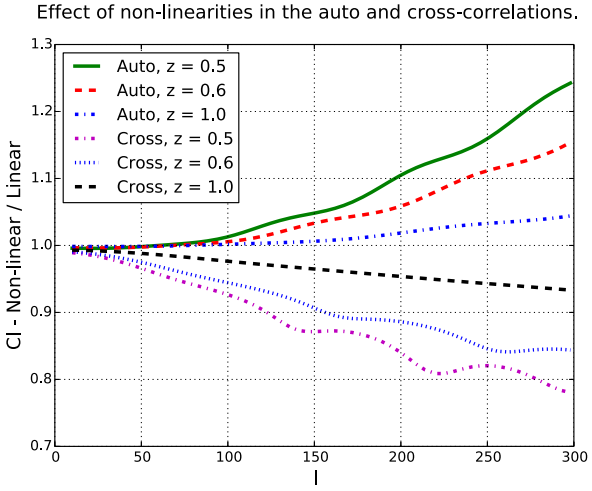

Figure A3. The impact of non-linear effect in the auto- and cross-correlations for different redshifts. The figure shows non-linear/linear correlation function ratio, with non-linear including Halofit contributions to the linear EH power spectrum. All redshift bins are $\Delta z = 0.01(1 + z)$ wide, the cross-correlation is with the adjacent bins and the redshifts $z = 0.5$, 0.6, 1.0 give the start of the first redshift bin.

As expected, the effect increases with l and lower redshifts have the highest non-linear contributions. The oscillations seen are due to the BAO. In the cross-correlations, the non-linear effects suppress the signal. Previously, we showed (Fig. 2) how counts–counts cross-correlations in narrow bins have both a positive and negative contribution from different scales. Since higher k-values contribute negatively and the non-linear effects increase with scale, this leads to non-linear effects suppressing the cross-correlations.

APPENDIX B: CC INTEGRATION

B1 Overview

The CC integration algorithm expands the integrand in Chebyshev polynomials and works well for oscillating integrals. Integrating f over the interval $[-1, 1]$ can be approximated as

$$\int_{-1}^{1} f(x)\,\mathrm{d}x \approx \sum_{n=0}^{N/2} \mathcal{W}_n f(\cos[n\pi/N]) + f(-\cos[n\pi/N]), \quad \text{(B1)}$$

where N is the number of integration points. The coefficients $\mathcal{W}_n$ are given by

$$d_i = \begin{cases} 1 & i = 0 \\ \frac{1}{1-N^2} & i = N/2 - 1 \\ \frac{1}{1-(2i)^2} & \text{Otherwise} \end{cases} \quad \text{(B2)}$$

$$D_{ij} = \frac{2}{N} \cos\left(\frac{2ij\pi}{N}\right) \quad \text{(B3)}$$

$$\mathcal{W} = D^{\mathrm{T}} d, \quad \text{(B4)}$$

where the last equation uses matrix multiplication. The integration in equation (B1) can be transformed to different integration limits. For example when integrating over scales, one has

$$\int_{k_{\min}}^{k_{\max}} f(k)\,\mathrm{d}k = k_w \int_{-1}^{1} f(\bar{k} + k_w x)\,\mathrm{d}x, \quad \text{(B5)}$$

where the integration variable is defined by $k = \bar{k} + k_w x$, $\bar{k} \equiv \frac{1}{2}(k_{\rm min} + k_{\rm max})$ and $k_w \equiv \frac{1}{2}(k_{\rm max} - k_{\rm min})$.

B2 Change of integral domain for the tomographic integration

The C_l integrand is of the form $f(x) \equiv G_i(x)G_j(x)$. When trying to integrate by multiplication, the expansion (B1) into two terms creates an additional complication. Expanding the terms, one finds

$$\int_{-1}^{1} G_i(x)G_j(x)\,{\rm d}x = \sum_{n=0}^{N/2} G_i(\cos(n\pi/N))G_j(\cos(n\pi/N)) + G_i(\cos(-n\pi/N))G_j\left(-\cos(n\pi/N)\right). \tag{B6}$$

Through defining

$$y^+_{in} = G_i(\cos(n\pi/N)) \tag{B7}$$

$$y^+_{jn} = G_i(-\cos(n\pi/N)) \tag{B8}$$

the integration can be written as

$$\int_{-1}^{1} G_i(x)G_j(x)\,{\rm d}x = \sum_n w_n \left(y^+_{in}y^+_{jn} + y^-_{in}y^-_{jn}\right). \tag{B9}$$

This paper has been typeset from a TEX/LATEX file prepared by the author.